Interfaces in ferroelastics: Fringing fields, microstructure, and size and shape effects

Marcel Porta
Departament d'Estructura i Constituents de la Matèria and Institut de Nanociència i Nanotecnologia, Universitat de Barcelona, Diagonal 647, 08028 Barcelona, Catalonia, Spain
and Department of Materials Science and Engineering, University of Toronto, Toronto, Canada M5S 3E4

Teresa Castán and Pol Lloveras
Departament d'Estructura i Constituents de la Matèria and Institut de Nanociència i Nanotecnologia, Universitat de Barcelona, Diagonal 647, 08028 Barcelona, Catalonia, Spain

Turab Lookman
Theoretical Division, Los Alamos National Laboratory, Los Alamos, New Mexico 87545, USA
and Department of Materials Science and Engineering, University of Toronto, Toronto, Canada M5S 3E4

Avadh Saxena
Theoretical Division, Los Alamos National Laboratory, Los Alamos, New Mexico 87545, USA

Subodh R. Shenoy
School of Physics, University of Hyderabad, Hyderabad 500046, India
(Received 28 October 2008; revised manuscript received 20 May 2009; published 29 June 2009)

We develop a strain-based approach to study the transformation of a finite martensite domain within an austenite host matrix. Analytical and numerical solutions are obtained for the fringing fields in the austenite and in the martensite and we test how well the stress and strain matching conditions are obeyed at the habit planes. We investigate the scaling of the energy of the fringing fields and show how simulations on relaxed microstructures corroborate the $1/|k_y|$ behavior for the energy in Fourier space. Our results show that the functional form $F=F_0+aL_1\xi+bLL_1/\xi$ for the total elastic energy provides an excellent fit to the numerical simulations, thus demonstrating that $\xi\sim\sqrt{L}$, where ξ is the twin width for a martensite region $L\times L_1$ with length of the habit plane L_1 and where $aL_1\xi$, bLL_1/ξ, and F_0 are the energies of the decaying strain field at the habit plane, twin-boundary energy, and energy of a single martensite variant, respectively. However, the result is only true for sufficiently large L and we provide insight into the breakdown of the $\xi\sim\sqrt{L}$ scaling at the nanoscale. Our approach allows us to investigate the effect of varying the *finite* distance between habit planes, L, and our key finding is that there is a minimum length, $L^{\min}$, for the nucleation of the twinned martensite structure which depends on temperature. As the temperature is lowered, $L^{\min}$ decreases, and at temperatures close to the *stability limit* of the austenite phase a *lattice martensite* structure in which the parent and product phases spatially alternate in a checker-board pattern is stable in a narrow region of the temperature versus L phase diagram. Such patterns have been seen at the nanoscale in lithium-based perovskites and inorganic spinels, as well as in coherent decomposition of precipitates in Co-Pt alloys. Finally, we show how the nature of the fringing fields due to an inclusion within an austenite matrix sensitively depends on its shape, size, and orientation and determines whether twinning or lattice martensite are the stable structures.

DOI: 10.1103/PhysRevB.79.214117 PACS number(s): 81.30.Kf, 64.70.Nd, 61.72.−y, 68.35.−p

I. INTRODUCTION

An understanding of elastic heterogeneity in strain-based materials, such as martensites, is key to describing and modeling interfaces and microstructure which influence constitutive behavior in shape memory applications.[1–4] Moreover, it provides a foundation for the study of functional materials, such as ferroelectrics, magnetoelastics, transition-metal oxides, e.g., perovskites and high-T_c cuprates, and magnetoelectrics, where functionalities such as polarization, magnetization, and charge can couple to lattice distortions.[5] The strain-mediated interactions can lead to heterogeneity of the functional phases[6,7] (coexistence of insulating and antiferromagnetic with conducting and magnetic) that have a bearing on the cross response due to applied fields, such as the effect of stress on magnetization.[8]

The structural transformations in ferroelastic crystals are diffusionless and, in the absence of external mechanical stress, such crystals possess two or more "orientation" or deformation states which can be mutually transformed from one to the other by means of mechanical stress.[9] These deformation states or variants typically occur due to a reduction in crystal symmetry in the course of the transformation, and hence the simplest elastic heterogeneities that arise are interfaces between the parent and product phases (habit planes) and between the product phases or variants themselves (twin boundaries or domain walls). These interfaces as well as aggregates of plane-parallel twins (e.g., polydomains) have been the subject of much interest over the last fifty years[10,11] since they were first observed by optical microscopy in In-Tl alloys.[12] The early theories on their descriptions were based

on the crystallographic theory of martensites where special deformation modes of twinning are invoked, in addition to the notion of an invariant plane of contact between the product and parent phases which was considered to be on average undistorted.

Over the last twenty years energy minimizing principles have been successfully employed to study elastic heterogeneities,[1,13,14] which are now viewed as the result of competition involving long-range elastic interactions[3,15,16] associated with structural domains (as distinct from deformation twinning), and this has given rise to a number of approaches based on some form of Landau theory.[17,18] Attention has also focused on the problem of the orientation of habit planes and twin boundaries. The strain-free criterion, that along all directions in the domain wall or habit plane the strains should be the same, has been extensively used[10,11,19] to obtain orientations of domain walls and habit planes of three dimensional crystals and more recently extended to all two-dimensional ferroelastic transformations.[20]

Although it was understood that twinning of the product phase (martensite) occurred in order to minimize the elastic energy arising from the matching to the parent phase (austenite), Horovitz *et al.*[21] were the first to perform a quantitative analysis of the energetics of a twin lattice in a host matrix to show how the twins can be stabilized by elastic interactions mediated by the austenite. They worked in a displacement-based picture and showed that decaying (fringing) fields in the austenite can be accompanied by twins of width ξ and length L in the martensite obeying the scaling relation $\xi \sim \sqrt{L}$. This was derived previously in a number of materials science studies using a variety of methods,[22] some of which either invoked the presence of dislocations[23] or did not use the effect of the long-range elastic interaction in an obvious manner.[24] Another point of view, based on the presence of vacancies at interfaces, was used to study the kinetics of growth of martensite variants.[25]

Our objective therefore is to study analytically and numerically the solutions for the elastic fields in the martensite phase due to a surrounding austenite matrix. We study this problem within a strain-based formalism in different martensite geometries. The advantage of using strain rather than displacement is that it serves as a natural order parameter (OP) in the context of Landau theory. Moreover, as the components of the strain tensor are derivatives of the displacement field for defect-free media and therefore satisfy an integrability condition such as the Saint-Venant's compatibility condition,[26] $\nabla \times [\nabla \times \varepsilon(\mathbf{r})]^{\dagger} = 0$, this naturally leads to long-range elastic interactions. We have previously shown that for an infinite system the non-OP strain components, which can be expressed in terms of the OP strain, play an essential role as they are responsible for the repulsive forces that arise by forcing strain compatibility at interfaces.[16] Using such a strain based description, we go beyond Ref. 21 in also studying the energetics in the martensite and show how the total-energy analysis leads to length scaling properties.

Our approach allows us to explore the fundamental question of how the microstructure crucially depends on the size of the transformed region. We perform simulations to show the behavior of the energy and fringing fields in the austenite away from the habit plane and in the martensite as a function of the size of the martensite domain. We numerically demonstrate that for sufficiently large domains the scaling is obeyed and show that a simple model in which the elastic energy of the fringing field competes with the energy of the twin boundary provides an excellent fit to the data. We show that a minimum size is required for twinned martensite (TM) to form and it depends on the temperature. Moreover, below a certain temperature and in a narrow range of the size of the transformed region, the twinned martensite decays to a heterogeneous (checker-board-type) structure containing both the parent and product phases. We discuss the stability of this *lattice martensite* (LM) and how it occurs in finite transformed regions, compared to infinite ones, and the influence of shape or geometry of the region on this structure. This checker-board-type structure containing thermodynamically inequivalent phases has been observed experimentally in the perovskite[27] $(Nd_{2/3-x}Li_{3x})TiO_3$, mixtures[28] of $ZnGa_2O_4$ and $ZnMn_2O_4$, or the ferromagnetic alloy[29] Co-Pt, systems in which strain is involved.

A recurring theme in this work that has not been explored previously in the study of polydomain or twinned martensite formation is the interplay of orientations of habit planes, fringing fields, microstructure, size, and shape and how it leads to novel features not typically associated with bulk martensite behavior. Moreover, the breakdown of the $\sqrt{L}$ scaling, which was observed to hold for coarse twins ($>\sim \mu$m) in InTl alloys,[12,21] has not been previously addressed. We provide insight into how and why this occurs as L is decreased below $\sim$50 nm.

Our work has relevance to understanding martensite behavior in nanocomposites where inclusions of transformable material are embedded in an austenite matrix. The size dependence of the martensitic transformation in nanocrystalline grains of NiTi alloys, which undergo a transformation from the cubic B2 phase to the monoclinic B19' martensite, has been investigated by Waitz and co-workers.[30] Using high-resolution transmission electron microscopy (HRTEM), they examined nanograins ranging in size from 5–350 nm that were obtained by devitrification of an amorphous phase by subjecting the alloys to severe plastic deformation and by using different heat treatments. Their results demonstrate that the nature of the transformed phase in the nanograins that are embedded in the amorphous or parent-type matrix varied with grain size. No martensite was observed for grain sizes below 60 nm; however, the B2 and R phases were observed. For grains below 15 nm, only the B2 phase was observed and for grains larger than 150 nm, the lattice structure was consistent with that of B19' phase with twinned widths of $\sim$20 nm, in contrast to the coarser twins observed in these alloys in bulk. These results do indicate that with decreasing grain size (and twin width) the strain and interfacial energy, the former affected by the confined region or boundary conditions associated with the grains, influence the stability of certain strain modes and hence the microstructure observed. Our results, within the context of a well-defined model geometry, and for a simpler transformation than that occurs in NiTi, are essentially consistent with these observations. We find a critical length scale below which twinned martensite gives rise to a different stable structure (lattice martensite), which is itself unstable if the size is reduced further and leads to an untransformed austenite.

The plan of the paper is as follows. In Sec. II we introduce the geometry of the austenite and martensite phase within an infinite domain with a given orientation, and the Landau-based model to be solved. The analytical expressions for the energy of the austenite and its effect on the strain fields in the martensite are obtained in Sec. III and the martensite energetics are derived in Sec. IV. Section V describes how the total-energy minimizing simulations are performed and we discuss our findings on the fringing fields, length scaling properties, and effects of small size on the transition temperature and microstructure. Section VI addresses how martensitic behavior is sensitive to finite domains and their geometry and a summary and discussion of the implications of this work are given in Sec. VII. Technical details of the strain fields in the austenite and martensite are relegated to Appendixes A and B, respectively.

II. MODEL

We consider a two-dimensional (2D) crystal undergoing a square-to-rectangular (SR) structural transformation.[15] The associated degrees of freedom are the lattice displacements, **u**, from which the strain tensor is defined. In linear elasticity it is given by

$$\varepsilon_{ij} = \frac{1}{2}\left(\frac{\partial u_i}{\partial r_j} + \frac{\partial u_j}{\partial r_i}\right), \tag{1}$$

where **r** is the position vector and i and j are Cartesian coordinates. In symmetrized form the strain components are the compressional, $e_1=(\varepsilon_{xx}+\varepsilon_{yy})/\sqrt{2}$, deviatoric, $e_2=(\varepsilon_{xx}-\varepsilon_{yy})/\sqrt{2}$, and shear, $e_3=\varepsilon_{xy}$ strains. The OP associated with the SR phase transformation is the deviatoric strain, e_2, and the three strain components are related through the elastic compatibility condition,[15]

$$(\partial_{xx}+\partial_{yy})e_1 - (\partial_{xx}-\partial_{yy})e_2 - \sqrt{8}\partial_{xy}e_3 = 0, \tag{2}$$

which arises from the fact that they are derivatives of the same underlying displacement field.

The geometry in 2D that forms the basis of our analytical study for martensite formation is a strip of finite width, L, and infinite length that forms the transformable region outside of which is the fixed austenite. In practice we construct the strip by defining a rectangular region of size $L\times L_1$ with periodic boundary conditions in the direction of length L_1 (Fig. 1). The orientation of side of length L_1 with respect to the crystallographic axes defines the orientation of the parent-product interface (habit plane).

In the central region with size $L\times L_1$, where the martensite phase is allowed to nucleate, the elastic energy associated with a distortion of the square lattice is described by means of a triple well Ginzburg-Landau potential in the OP, e_2,

$$f_{GL} = \frac{A}{2}(T-T_c)e_2^2 - \frac{B}{4}e_2^4 + \frac{C}{6}e_2^6 + \frac{\kappa}{2}|\nabla e_2|^2, \tag{3}$$

augmented with the harmonic contribution of the compressional-shear (CS) strains,[15]

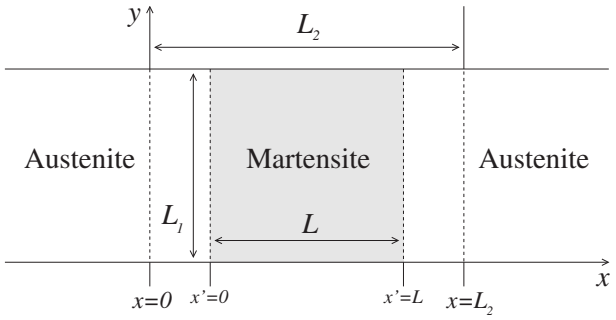

FIG. 1. Geometry showing the transformable or martensite phase embedded in an austenite matrix. The region is divided into an outer domain defined by $x<0$ and $x>L_2$ and an inner domain of size $L_2\times L_1$. The latter is made of the martensite region of size $L\times L_1$, within which the free-energy potential is nonlinear, and the regions enclosed within $x>0$ and $x'<0$ and $x'>L$ and $x<L_2$. The Landau free energy for the OP strain e_2 [Eqs. (3) and (5)] is not continuous at the habit planes $x'=0$ and $x'=L$ as it is only harmonic in the austenite region.

$$f_{CS} = \frac{A_1}{2}e_1^2 + \frac{A_3}{2}e_3^2, \tag{4}$$

so that the free-energy density of the martensite is $f_{\text{mar}}=f_{GL}+f_{CS}$. Outside this central region the system is constrained to be in the austenite phase by using a harmonic free energy in the symmetry adapted strains,[21]

$$f_{\text{aus}} = \frac{A_1}{2}e_1^2 + \frac{A_2}{2}e_2^2 + \frac{A_3}{2}e_3^2, \tag{5}$$

with $A_2=A(T-T_c)$. The elastic constant A_2 varies linearly with temperature and A is the change in elastic constant per unit change in temperature. The elastic constants A_1 and A_3 are of second order, and B and C are higher-order elastic constants. We are considering the elastic constants at the harmonic level to be the same for austenite and martensite for simplicity, but these can be different for distinct materials. The coefficient κ is the energy cost of creating variations in the OP.

For the solution of this problem, it is convenient to divide the system into a region of size $L_2\times L_1$ (hereafter to be referred to as the "inner domain") and an "outer domain" defined by $x<0$ and $x>L_2$ (Fig. 1). The former includes the transformation region of size $L\times L_1$, where the free-energy potential is nonlinear, and the regions enclosed within $x>0$ and $x'<0$, and $x'>L$ and $x<L_2$. At the semi-infinite boundaries $x=0$ and $x=L_2$ (which we will refer to as "matching planes"), the Landau free energies are continuous and all three strain components are perfectly matched on either side of them. However, at the habit planes $x'=0$ and $x'=L$ that separate the austenite and martensite phases, the Landau free energy is not continuous in terms of the OP strain, e_2, as it is harmonic in the regions $x'<0$ and $x'>L$ and nonlinear within the region defined by $x'>0$ and $x'<L$. Thus, the outer domain is characterized by elastic energy contributions harmonic in all of the strains e_1, e_2, and e_3, whereas only e_1 and e_3 are harmonic in the inner domain.

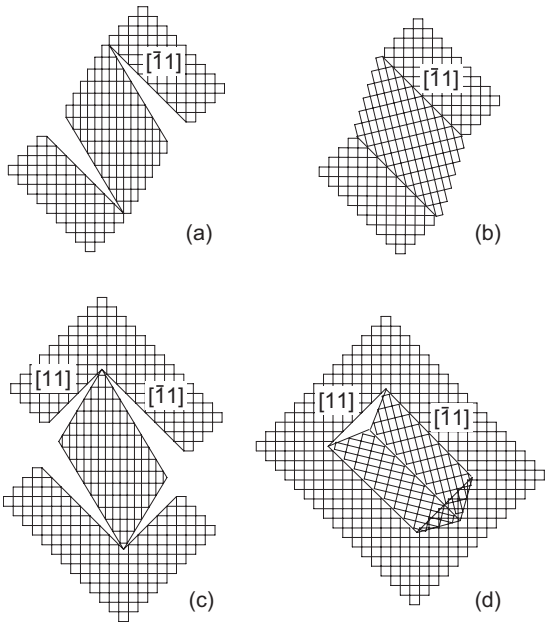

FIG. 2. Schematic representation of the matching between the austenite and the martensite phases for the SR (Square to Rectangle) structural transformation before strain accommodation by relaxation. Different geometries are considered. (a) Formation of a single martensite plate of finite width and infinite length between two austenite phases, with the habit planes oriented in [$\bar{1}$1] direction. (b) A rotation of the martensite plate allows the coherent matching to the austenite phases. (c) Formation of a single martensite plate of finite width and finite length within an austenite matrix. Different rotation angles are needed for the matching of the habit planes oriented in [11] and [$\bar{1}$1] directions. (d) Formation of a twinned martensite phase within an austenite matrix. A microscopic misfit at the habit plane oriented in [11] direction needs to be accommodated.

A. Orientation of habit plane and twin boundary

Following the work of Sapriel,[10,19] Roytburd[10,11] and others,[20] a single martensite variant can be coherently matched to the austenite phase for an SR transformation provided the habit plane is oriented along the [11] direction. A rotation of one phase with respect to the other is also required for the matching to hold[10,11] [Figs. 2(a) and 2(b)]. Therefore, if the habit planes in Fig. 1 have this orientation, the ground state corresponding to this geometry is a single martensite variant matched to the austenite phase. However, a single martensite plate of *finite* length cannot be coherently matched to a surrounding austenite matrix as the habit planes along the [11] and [$\bar{1}$1] directions require different rotation angles of the martensite plate [Fig. 2(c)]. The mechanism that allows for the matching between both phases is the twinning of the martensite plate along the [11] direction [Fig. 2(d)]. This leads to a habit plane along [11] direction which is a macroscopically invariant plane, but where microscopically there is a misfit between the parent and product phases. The accommodation of this misfit generates decaying strain fields which crucially determine the microstructure of the martensite. For an SR transformation, provided the fraction of the two martensite variants is equal, the average strain in any plane crossing the twinned martensite will vanish.[11] Therefore all such planes are macroscopically invariant planes and can play the role of the habit plane in Fig. 1. Thus, in order to study the properties of the decaying strain fields and their influence on the microstructure of the martensite using the geometry described in Fig. 1, we choose in this work an orientation for the habit planes that is different from the [11] direction. This avoids the formation of a single martensite variant in this infinite system and forces twinning. The habit planes in Fig. 1 are chosen to be parallel to the [01] crystallographic direction.

III. OUTER DOMAIN SOLUTION INVOLVING AUSTENITE

Our approach to obtaining a solution to the model and geometry above is to first consider the outer domain containing austenite only in the regions $x<0$ and $x>L_2$ and obtain the strains and energy in these regions. We will show that the effects of the outer domain manifest as constraints on the strains at the matching planes $x=0$ and $x=L_2$, which will subsequently be taken into account in solving the inner domain problem in the region $0<x<L_2$. Here we obtain the analytical expressions for the strain fields in the outer domain which in turn will provide insight into the nature of the *coherent* matching of the austenite to the martensite. In contrast to the approach in terms of displacements previously employed for the austenite,[21] we will use a strain-based description in which the compatibility of the strain components is enforced. The strain field that minimizes the elastic energy of the outer domain is obtained by demanding mechanical equilibrium,[31] $\nabla\cdot\sigma=0$, where σ is the stress tensor. This condition, together with elastic compatibility [Eq. (2)] and the requirement that the strain field vanishes far from the habit plane, defines a boundary-value problem. The complete solution to this problem is given in Appendix A for an outer domain in the region $x>0$. The corresponding results for $x<0$ and $x>L_2$ are then obtained by applying the transformations $x\rightarrow -x$ and $x\rightarrow x-L_2$, respectively.

A. Solution of the boundary-value problem for $x>0$

Mechanical equilibrium requires that the elastic force on each small volume of the system vanishes. In terms of the stress tensor, σ_{ij}, the force is given by

$$f_i=\sum_j \frac{\partial\sigma_{ij}}{\partial x_j}, \tag{6}$$

where i and j are Cartesian coordinates. In 2D this gives rise to two equations,

$$f_x=\partial_x\sigma_{xx}+\partial_y\sigma_{xy}=0,$$

$$f_y=\partial_x\sigma_{yx}+\partial_y\sigma_{yy}=0. \tag{7}$$

The stress tensor is related to the elastic free-energy density, f, through

$$\sigma_{ij} = \frac{\partial f}{\partial \varepsilon_{ij}}. \tag{8}$$

Thus, for the harmonic free energy corresponding to square symmetry [Eq. (5)], we obtain

$$A_1 \partial_x e_1 + A_2 \partial_x e_2 + \frac{A_3}{\sqrt{2}} \partial_y e_3 = 0,$$

$$A_1 \partial_y e_1 - A_2 \partial_y e_2 + \frac{A_3}{\sqrt{2}} \partial_x e_3 = 0. \tag{9}$$

In addition, the strain field must satisfy elastic compatibility so that Eqs. (2) and (9), together with the conditions of continuity across the matching plane and the vanishing of the strain field far from it, define a boundary-value problem. Transforming the set of differential equations by Laplace in x direction and Fourier in y direction gives rise to the set of algebraic equations,

$$A_1[q\tilde{e}_1 - \hat{e}_1(0)] + A_2[q\tilde{e}_2 - \hat{e}_2(0)] - ik_y \frac{A_3}{\sqrt{2}} \tilde{e}_3 = 0,$$

$$-ik_y A_1 \tilde{e}_1 + ik_y A_2 \tilde{e}_2 + \frac{A_3}{\sqrt{2}}[q\tilde{e}_3 - \hat{e}_3(0)] = 0,$$

$$(q^2 - k_y^2)\tilde{e}_1 - q\hat{e}_1(0) - \partial_x \hat{e}_1(0) - (q^2 + k_y^2)\tilde{e}_2 + q\hat{e}_2(0) + \partial_x \hat{e}_2(0) + ik_y \sqrt{8}[q\tilde{e}_3 - \hat{e}_3(0)] = 0, \tag{10}$$

where the Fourier-Laplace transform is defined by

$$\tilde{e}_\alpha(q, k_y) = \int_0^{+\infty} e^{-qx} \hat{e}_\alpha(x) dx, \tag{11}$$

where $\hat{e}_\alpha(x)$ is the Fourier transform of $e_\alpha(x,y)$ with respect to y, defined by

$$\hat{e}_\alpha(x) = \frac{1}{L_1} \int_0^{L_1} e^{ik_y y} e_\alpha(x,y) dy, \tag{12}$$

and $\hat{e}_\alpha(0)$ and $\partial_x \hat{e}_\alpha(0)$ are the Fourier transforms with respect to y of the strain field and its derivative with respect to x, respectively, evaluated at the $x=0$ plane.[16,21] As shown in Appendix A, the solution to Eq. (10) has the form

$$\hat{e}_2(x) = C_1 \exp[(C_\beta + i\beta)|k_y|x] + C_2 \exp[(C_\beta - i\beta)|k_y|x] + C_3 \exp[(-C_\beta + i\beta)|k_y|x] + C_4 \exp[(-C_\beta - i\beta)|k_y|x], \tag{13}$$

where $\beta^2 = A_1(A_3 - 2A_2)/[A_3(A_1 + A_2)]$ and $C_\beta = \sqrt{1-\beta^2}$. The requirement that the strain field vanishes far from the matching plane imposes $C_1 = C_2 = 0$. These constraints can be written as

$$\hat{e}_3(0) = \frac{i\sqrt{2}}{C_\beta} \frac{A_2}{A_3} \frac{k_y}{|k_y|} \hat{e}_2(0), \tag{14}$$

$$\partial_x \hat{e}_1(0) - \partial_x \hat{e}_2(0) = \frac{|k_y|}{A_3 C_\beta}[-(2A_1 + A_3)\hat{e}_1(0) + 2A_2 \hat{e}_2(0)]. \tag{15}$$

When these constraints are taken into account, the solution of the boundary-value problem for the three fields is (see Appendix A for details)

$$\hat{e}_1(x) = \left[\hat{e}_1(0)\cos(\beta|k_y|x) - \frac{\beta}{C_\beta} \frac{A_2}{A_1} \hat{e}_2(0)\sin(\beta|k_y|x) \right] \times \exp(-C_\beta |k_y| x),$$

$$\hat{e}_2(x) = \left[\frac{C_\beta}{\beta} \frac{A_1}{A_2} \hat{e}_1(0)\sin(\beta|k_y|x) + \hat{e}_2(0)\cos(\beta|k_y|x) \right] \times \exp(-C_\beta |k_y| x),$$

$$\hat{e}_3(x) = \frac{i\sqrt{2}}{A_3} \frac{k_y}{|k_y|} \left[\frac{A_1}{\beta} \hat{e}_1(0)\sin(\beta|k_y|x) + \frac{A_2}{C_\beta} \hat{e}_2(0)\cos(\beta|k_y|x) \right] \times \exp(-C_\beta |k_y| x). \tag{16}$$

The elastic energy of the outer domain containing austenite can now be evaluated, leading to

$$F^{\text{out}} = \int_0^\infty dx \int_0^{L_1} dy f_{\text{aus}} = \frac{L_1}{2} \sum_{k_y} \frac{1}{|k_y|} \times \left\{ \frac{(A_1 + A_2)A_1 C_\beta}{2A_2} |\hat{e}_1(0)|^2 + \frac{A_2(2A_2 + A_3)}{2A_3 C_\beta} |\hat{e}_2(0)|^2 + \frac{A_1 A_2}{A_3 C_\beta} [\hat{e}_1(0)\hat{e}_2^*(0) + \hat{e}_1^*(0)\hat{e}_2(0)] \right\}. \tag{17}$$

The $1/|k_y|$ factor in Eq. (17) indicates that the energy within the outer domain would diverge unless the fractions of the different martensitic variants at the matching plane are equal. This ensures that, on average, the strain vanishes at this plane and lattice integrity can be preserved. Moreover, this term favors short-wavelength modulations of the strain, or equivalently, the formation of narrow twins.

The general conditions that must be satisfied at the matching plane are the continuity of the displacements, which is guaranteed by elastic compatibility, and the continuity of the traction.[32] The latter is defined as the force per unit surface area acting at the plane with components given by

$$\tau_i = \sum_j \sigma_{ij} \hat{n}_j, \tag{18}$$

where σ_{ij} are the components of the stress tensor and $\hat{n}$ is a unit vector normal to the plane. It can be understood as an integral of $\nabla \cdot \sigma = 0$ in a pill-box volume across the surface, using Gauss's theorem. For the $x=0$ plane, $\hat{n} = (10)$, and thus the continuity of the traction across this plane requires the continuity of the components σ_{xx} and σ_{xy} of the stress tensor.

Across the matching plane $x=0$, the Landau free-energy density is continuous, and therefore the three strain (and stress) components are continuous, as they are the solution of the system of differential equations defined by mechanical equilibrium [Eq. (9)] and elastic compatibility [Eq. (2)]. In

addition, the derivatives $\partial_x e_1$ and $\partial_x e_2$ entering in the constraint given by Eq. (15) are also continuous. Hence, the continuity of $\partial_x e_2$ allows us to determine the compressional strain at the matching plane since differentiation of Eq. (16) gives

$$\hat{e}_1(0) = \frac{A_2}{A_1}\left[\hat{e}_2(0) + \frac{1}{C_\beta |k_y|}\partial_x \hat{e}_2(0)\right]. \tag{19}$$

By using Eq. (19) all the strain components can be written in terms of the OP, e_2, and its gradient, $\partial_x e_2$, at the matching plane. In addition, at the matching plane e_1, e_3 and $\partial_x e_1$ are given by Eqs. (14) and (19) and

$$\partial_x \hat{e}_1(0) = -\frac{A_2}{A_1}\left[\frac{|k_y|}{C_\beta}\hat{e}_2(0) + \partial_x \hat{e}_2(0)\right], \tag{20}$$

which follows from Eqs. (15) and (19). These form the boundary conditions for the inner domain solution.

In terms of $\hat{e}_2(0)$ and $\partial_x \hat{e}_2(0)$, the elastic energy of the austenite phase in the outer domain $x>0$ becomes

$$F^{\text{out}} = \frac{L_1}{2}\sum_{k_y}\left\{\frac{A_2[8A_1A_2 + (A_1+A_2)A_3]}{2A_1A_3C_\beta}\frac{1}{|k_y|}|\hat{e}_2(0)|^2 + \frac{(4A_1+A_3)A_2^2}{2A_1A_3C_\beta^2}\frac{1}{k_y^2}[\hat{e}_2(0)\partial_x \hat{e}_2^*(0) + \hat{e}_2^*(0)\partial_x \hat{e}_2(0)] + \frac{(A_1+A_2)A_2}{2A_1C_\beta}\frac{1}{|k_y|^3}|\partial_x \hat{e}_2(0)|^2\right\}. \tag{21}$$

B. Outer domain for $x<0$

The corresponding expressions for $x<0$ (Fig. 1) are obtained by applying the transformation $x \to -x$ on the results obtained for $x>0$. We note that the shear strain, which is defined in terms of displacement gradients, $e_3 \equiv \varepsilon_{xy} = \frac{1}{2}(\partial u_x/\partial y + \partial u_y/\partial x)$ is an odd function with respect to this transformation, and thus its sign changes. On the contrary, e_1 and e_2 are even functions, and their signs remain invariant. The constraints on the strains at the matching plane $x=0$ are therefore

$$\hat{e}_1(0) = \frac{A_2}{A_1}\left[\hat{e}_2(0) - \frac{1}{C_\beta |k_y|}\partial_x \hat{e}_2(0)\right], \tag{22}$$

$$\partial_x \hat{e}_1(0) = \frac{A_2}{A_1}\left[\frac{|k_y|}{C_\beta}\hat{e}_2(0) - \partial_x \hat{e}_2(0)\right], \tag{23}$$

$$\hat{e}_3(0) = -\frac{i\sqrt{2}}{C_\beta}\frac{A_2}{A_3}\frac{k_y}{|k_y|}\hat{e}_2(0). \tag{24}$$

C. Outer domain for $x>L_2$

The results for $x>L_2$ are obtained by applying the transformation $x \to x-L_2$ on the results obtained for $x>0$. The constraints on the strains at the matching plane $x=L_2$ are

$$\hat{e}_1(L_2) = \frac{A_2}{A_1}\left[\hat{e}_2(L_2) + \frac{1}{C_\beta |k_y|}\partial_x \hat{e}_2(L_2)\right], \tag{25}$$

$$\partial_x \hat{e}_1(L_2) = -\frac{A_2}{A_1}\left[\frac{|k_y|}{C_\beta}\hat{e}_2(L_2) + \partial_x \hat{e}_2(L_2)\right], \tag{26}$$

$$\hat{e}_3(L_2) = \frac{i\sqrt{2}}{C_\beta}\frac{A_2}{A_3}\frac{k_y}{|k_y|}\hat{e}_2(L_2). \tag{27}$$

IV. INNER DOMAIN SOLUTION INVOLVING MARTENSITE

The outer domain solution above forms the basis for obtaining the strain fields and energy in the inner domain that includes the transformable or martensite region (Fig. 1). We will again formulate this problem within a strain based description and show how the solution leads to an understanding of the formation of twinned microstructure in a simplified mode analysis. Full numerical solutions to the equations obtained here will be considered in Sec. V. We describe the procedure followed to obtain the compressional-shear energy in this region [see Eq. (4)],

$$F_{CS}^{\text{in}} = \int_0^{L_2} dx \int_0^{L_1} dy f_{CS}. \tag{28}$$

The details of the calculation are given in Appendix B. The goal is to obtain the result in terms of the OP only. To this end, the compressional strain is expressed in terms of the deviatoric and shear strains, using elastic compatibility [Eq. (2)]. The resulting elastic energy is then minimized with respect to the shear strain, taking into account the constraints at the matching planes given by Eqs. (22)–(27).

The result is given in terms of the coefficients of the cosine Fourier series (with respect to x) of $\hat{e}_2(x)$,

$$\hat{e}_2^{(n)} = \frac{2}{L_2}\int_0^{L_2} \hat{e}_2(x)\cos(k_x x)dx, \tag{29}$$

where $k_x = \pi n/L_2$ with n an integer. We obtain

$$F_{CS}^{\text{in}} = \frac{L_1L_2}{2}\sum_{k_y}\left\{\frac{A_1}{4}\left|-\hat{e}_2^{(0)} + \frac{1}{|k_y|L_2}\Phi^{(0)}\right|^2 + \sum_{n\neq 0}\frac{\frac{1}{2}A_1A_3}{8A_1k_x^2k_y^2 + A_3(k_x^2+k_y^2)^2}\left|(k_x^2-k_y^2)\hat{e}_2^{(n)} + \frac{|k_y|}{L_2}\Phi^{(n)}\right|^2 + \frac{\sqrt{A_3(2A_1+A_3)}}{2L_2}\frac{1}{|k_y|}\left[\left|-\frac{1}{2}\hat{e}_2^{(0)} + \sum_{n\ \text{even}(\neq 0)}\frac{A_3(k_x^2-k_y^2)(k_x^2+k_y^2)}{8A_1k_x^2k_y^2 + A_3(k_x^2+k_y^2)^2}\hat{e}_2^{(n)} + \Psi^e\right|^2 + \left|\sum_{n\ \text{odd}}\frac{A_3(k_x^2-k_y^2)(k_x^2+k_y^2)}{8A_1k_x^2k_y^2 + A_3(k_x^2+k_y^2)^2}\hat{e}_2^{(n)} + \Psi^o\right|^2\right]\right\}, \tag{30}$$

where $\Phi^{(n)}$, Ψ^e, and Ψ^o are functions of the OP and its gradient at the matching planes, $x=0$ and $x=L_2$,

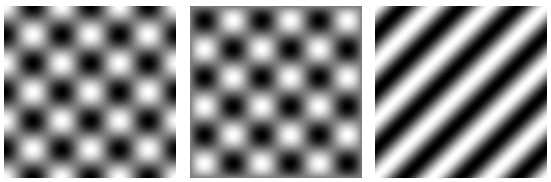

FIG. 3. (a) Deviatoric strain field A given by Eq. (32) for $\theta=0$. (b) Strain field B obtained from (a) by means of the displacement given by $\mathbf{r}=\pi(1,1)/(2k_0)$. (c) Superposition of the strain fields shown in (a) and (b).

$$\Phi^{(n)} = -\frac{2A_2(4A_1+A_3)}{A_1A_3C_\beta}[\hat{e}_2(0)+(-1)^n\hat{e}_2(L_2)] + \frac{2(A_1+A_2)}{A_1}\frac{1}{|k_y|}[\partial_x\hat{e}_2(0)-(-1)^n\partial_x\hat{e}_2(L_2)],$$

$$\Psi^e = -\frac{A_2}{2A_1}\left[1+\frac{4A_1+A_3}{C_\beta\sqrt{(2A_1+A_3)A_3}}\right][\hat{e}_2(0)+\hat{e}_2(L_2)] + \frac{1}{2A_1}\left[\frac{A_2}{C_\beta}+\frac{(A_1+A_2)A_3}{\sqrt{(2A_1+A_3)A_3}}\right]\frac{\partial_x\hat{e}_2(0)-\partial_x\hat{e}_2(L_2)}{|k_y|},$$

$$\Psi^o = -\frac{A_2}{2A_1}\left[1+\frac{4A_1+A_3}{C_\beta\sqrt{(2A_1+A_3)A_3}}\right][\hat{e}_2(0)-\hat{e}_2(L_2)] + \frac{1}{2A_1}\left[\frac{A_2}{C_\beta}+\frac{(A_1+A_2)A_3}{\sqrt{(2A_1+A_3)A_3}}\right]\frac{\partial_x\hat{e}_2(0)+\partial_x\hat{e}_2(L_2)}{|k_y|}. \tag{31}$$

We now clarify the essential physics underlying this result by obtaining a simplified form for the strains using a single-mode approximation appropriate for $L_2\approx L$ (Fig. 1) and show how this leads to an understanding of the twinned microstructure. Disregarding the contribution of the terms $\Phi^{(n)}$, Ψ^e, and Ψ^o localized at the matching planes, the elastic energy contains the essential form, $(k_x^2-k_y^2)^2\hat{e}_2^{(n)}\hat{e}_2^{(n)*}$, where we recall that $\hat{e}_2^{(n)}$ is the complex Fourier transform in the y direction and the cosine Fourier transform in the x direction of $e_2(x,y)$. This favors modulations of the deviatoric strain with $k_y=\pm k_x$ so that a single-mode OP strain field with this proper orientation of the wave vector $[\mathbf{k}=(k_0,\pm k_0)]$ (strain field A) is given by

$$e_2(x,y) = \rho[e^{i\theta}e^{ik_0y}+e^{-i\theta}e^{-ik_0y}]\cos(k_0x) = 2\rho\cos(k_0y+\theta)\cos(k_0x), \tag{32}$$

where ρ and θ are real constants. We note that since $e_2(x,y)\in\Re$ and $k_x>0$ the simultaneous contribution of $k_y=\pm k_x$ is needed, and thus strain field A is modulated in [11] and $[\bar{1}1]$ directions at the same time. This OP field is plotted in Fig. 3(a) for $\theta=0$. Since the terms $(k_x^2-k_y^2)\hat{e}_2^{(n)}$ vanish for all $\mathbf{k}$, the CS free energy depends only on the terms localized at the matching planes, $\Phi^{(n)}$, Ψ^e, and Ψ^o. Therefore, this CS free energy must be associated with a fringing field emanating from the matching plane (or the habit plane, since the single-mode approximation for the OP strain is only appropriate for $L_2\approx L$). That is, the compressional and shear strains corresponding to strain field A must vanish far from the habit planes. These strain fields can be computed from the OP strain field (see Appendix B for details) and are shown in the upper (compressional strain) and lower (shear strain) panels of Fig. 4(a).

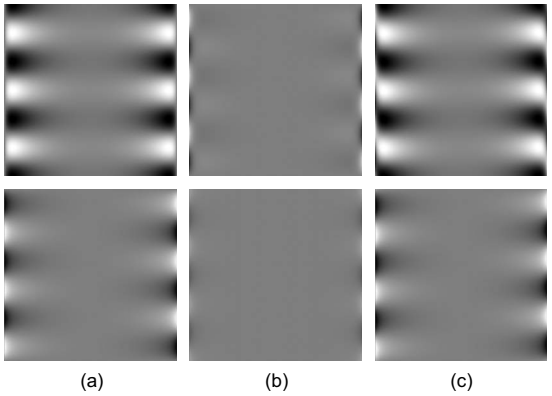

FIG. 4. Compressional (upper panel) and shear (lower panel) strain fields corresponding to the deviatoric strain fields shown in Fig. 3.

On the other hand, in the bulk the elastic energy must be invariant to a global translation of the OP field. In particular, it must be invariant to the translation given by the vector $\mathbf{r}=\pi(1,1)/(2k_0)$, which transforms strain field A [Eq. (32)] into the strain field,

$$e_2(x,y) = 2\rho\sin(k_0y+\theta)\sin(k_0x). \tag{33}$$

This function (strain field B) is plotted in Fig. 3(b) for $\theta=0$. Because the bulk energy must be invariant to the applied translation, the compressional and shear strain fields associated with strain field B must also vanish far from the habit planes. These are plotted in Fig. 4(b).

The complex-cosine transformation of strain field B (where $k_0=\pi n/L_2$) is

$$\hat{e}_2^{(m)}(\bar{k}_y) = \frac{2\rho}{iL_2}\left[\frac{k_0}{k_0^2-\bar{k}_x^2}(1-(-1)^{n+m})\right] \times[e^{i\theta}\delta_{\bar{k}_y,-k_0}^{-}-e^{-i\theta}\delta_{\bar{k}_y,k_0}^{-}], \tag{34}$$

where $\bar{k}_x=\pi m/L_2$. Thus, according to Eq. (30), strain field B has a contribution to the CS free energy from both the terms $\Phi^{(m)}$, Ψ^e, Ψ^o, and $(\bar{k}_x^2-\bar{k}_y^2)\hat{e}_2^{(m)}$ with $\bar{k}_y\neq\pm\bar{k}_x$. Nevertheless, as we have seen above, this energy contribution is localized in the neighborhood of the habit planes.

The superposition of strain field A and strain field B yields the plane wave shown in Fig. 3(c), which also has a vanishing contribution to the CS free energy far from the habit planes [see Fig. 4(c)]. In this way we recover the result corresponding to an infinite system, where the CS free energy vanishes provided that the wave vector is properly oriented in the [11] direction.[15] In a martensite phase embedded in an austenite matrix where the bulk term is dominant, we thus

expect a twinned martensite structure in either [11] or $[\bar{1}1]$ direction with a fringing field in the vicinity of the habit planes.

The next step is to analyze the scaling relations of the fringing field. For a plane wave $e^{i|k_y|(x\pm y)}$, such as that shown in Fig. 3(c), the gradient of the OP at the matching planes scales as $\partial_x \hat{e}_2(x) \sim |k_y|$. Therefore, the terms $\Phi^{(n)}$, Ψ^e, and Ψ^o do not depend explicitly on k_y [see Eq. (31)]. On the other hand, from Eq. (34) we obtain the scaling relation $(k_x^2 - k_y^2)\hat{e}_2^{(n)} \sim |k_y|/L_2$. Thus, both the elastic energy in the outer domain (austenite) [Eq. (21)] and the CS energy in the inner domain (martensite) [Eq. (30)] scale as[33] $F^{\text{out}} \sim F_{CS}^{\text{in}} \sim 1/|k_y|$ and are independent of the distance between matching planes, L_2, or habit planes, L (for $L_2 \approx L$).

A twinned martensite structure with the proper orientation of the twin boundaries in [11] direction is essentially a superposition of modes, in order to reduce the energy of the associated fringing field, in both the austenite and the martensite phases. In Sec. V we will show numerically that the elastic energy of the fringing field of a fully relaxed martensite phase also satisfies the scaling relation $F^{\text{out}} \sim F_{CS}^{\text{in}} \sim 1/|k_y|$ and is independent of the distance between habit planes, L.

V. SIMULATION RESULTS: ENERGY MINIMIZED MICROSTRUCTURE AND STRAIN FIELDS

Equilibrium strain configurations corresponding to the model presented above are obtained by minimizing the total free energy, F, the sum of the outer and inner contributions, using the relaxational equation,

$$\frac{\partial e_2}{\partial t} = -\gamma \frac{\delta F/\delta e_2}{\alpha^2 + |\delta^2 F/\delta e_2^2|}, \tag{35}$$

where γ corresponds to a mobility which is taken to be 1. Thus, the analytical results of the outer domain energy and the CS free energy of the inner domain are included in the minimization as they can be a dominant contribution. The second derivative of the free energy in the denominator has been introduced empirically in order to speed up the relaxation process, as it effectively adapts the integration time step, $dt' \equiv dt/(\alpha^2 + |\delta^2 F/\delta e_2^2|)$, to the topology of the free-energy functional. The parameter α was initially introduced to avoid numerical problems in case that the second derivative of the free energy vanishes. However, we did not find numerical instabilities for small values of α, so that we set $\alpha = 0$. This relaxational equation is useful when the convexity of the free energy as a function of the local strain variables strongly depends on which part of the system is being relaxed or evolved in time.

Because the free energy of the outer domain depends only on the deviatoric strain at the matching planes, the free energy of the model currently studied is much more sensitive to changes close to these planes than in the bulk. The functional derivative of the free energy with respect to the variable $\eta_-(y) \equiv e_2(x=\Lambda, y) - e_2(x=0, y)$, used to estimate the strain gradient at the matching plane, $\partial_x e_2(x=0, y) \approx \eta_-(y)/\Lambda$, where Λ is the discretization parameter, is orders of magnitude larger than the functional derivative with respect to $\eta_+(y) \equiv e_2(x=\Lambda, y) + e_2(x=0, y)$. Therefore, the topology of the free energy as a function of the variables $e_2(x=\Lambda, y)$ and $e_2(x=0, y)$ is a minimum that is elongated in the [11] direction along the line $\eta_-(y) = \text{constant}$. In this topology it is more efficient to minimize the free energy with respect to the variables $\eta_\pm(y)$ rather than with respect to the local strains. Thus, we define

$$\frac{\partial \eta_\pm(y)}{\partial t} = -\gamma \frac{\delta F/\delta \eta_\pm(y)}{|\delta^2 F/\delta \eta_\pm^2(y)|}, \tag{36}$$

and the time evolution of the strain variables $e_2(x=\Lambda, y)$ and $e_2(x=0, y)$ localized in the vicinity of the $x=0$ matching plane is obtained from the time evolution of $\eta_\pm(y)$. This method is more efficient because the effective time step $dt' \equiv dt/|\delta^2 F/\delta \eta_+^2(y)|$ corresponding to the variable $\eta_+(y)$ can be much larger than if Eq. (35) is used. Additionally, different time steps, dt, have been used for the variables $\eta_+(y)$, $\eta_-(y)$, and $e_2(x, y)$ in the bulk. The same method has been applied to evaluate the time evolution of the variables $e_2(x = L_2 - \Lambda, y)$ and $e_2(x=L_2, y)$ localized in the vicinity of the $x=L_2$ matching plane. Within the inner domain (Fig. 1) the Landau free energy is defined to be harmonic in the deviatoric strain only at $x=0$, $x=\Lambda$, $x=L_2-\Lambda$, and $x=L_2$, where the strain is used for the computation of the energy of the outer domain (at $x<0$ and $x>L_2$). In the remaining points of the inner domain the Landau free energy is nonlinear [Eq. (3)].

The model parameters used throughout the paper are the values for FePd.[15] The results will be presented in terms of $A = 2.4 \times 10^8$ N/Km^2, $T_c = 257$ K, and $\kappa = 3.5306 \times 10^{-9}$ N, which define the units of energy, length, and temperature. In terms of these reduced units the remaining parameters are: $B = 275.62$, $C = 4.864 \times 10^5$, $A_1 = 2.2698$, and $A_3 = 4.5396$, and the unit of length is $\ell = \sqrt{\kappa/T_c A} = 0.239\,25$ nm. The size of the simulated system ranges from $L_2 \times L_1 = 15\ell \times 240\ell$ to $4000\ell \times 4000\ell$, and has been discretized onto a mesh of size ranging from 32×512 to 1024×1024, with a discretization parameter ranging from $\Lambda = 0.47\ell$ to 7.8ℓ, depending on temperature. Periodic boundary conditions are used in the y direction as the geometry of Fig. 1 is considered infinite in that direction but the system is of finite extent ($=L_2$) in the x direction.

The relaxation of an initially disordered configuration using Eqs. (35) and (36) does not break the global square symmetry in most cases but a metastable checker-board-like phase with coexisting martensite variants and austenite is obtained. Therefore, a small amount of quenched disorder is introduced in the Landau free energy coupled to the OP through the harmonic term, akin to introducing a spatially dependent transition temperature. Once the square symmetry is broken into rectangular symmetry, the disorder is removed, and the nucleated martensite phase relaxes into a twinned martensite structure where all the twins have the same width. In order to save computation time, the initial configurations used when studying the properties of the twinned martensite structure are equal-width twin structures with a constant value of the strain, $e_2(x, y) = \pm \varepsilon_0$, where ε_0 is the strain

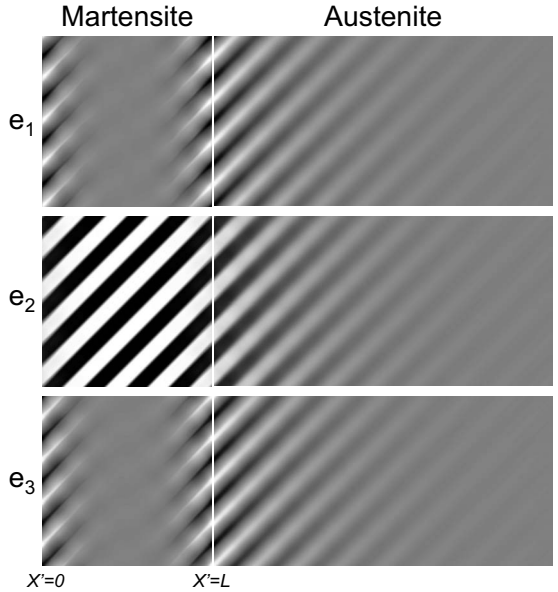

FIG. 5. Strain fields of a fully relaxed twinned martensite phase embedded in an austenite matrix at $T=1.01T_c$, using periodic boundary conditions in the y direction. Grey corresponds to the unstrained structure, whereas black (white) corresponds to a negative (positive) strain.

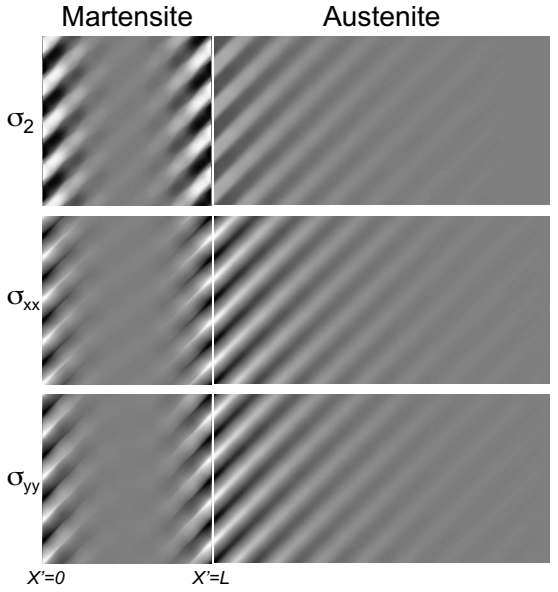

FIG. 6. Stress fields corresponding to the strain fields shown in Fig. 5. Grey corresponds to the stress free structure, whereas black (white) corresponds to a negative (positive) stress. The discontinuity in $\sigma_2=(\sigma_{xx}-\sigma_{yy})/\sqrt{2}=\partial f/\partial e_2$ arises from the discontinuity of the Landau free energy at the habit plane, and σ_{xx} is continuous.

which minimizes the Landau free energy at a given temperature. The application of Eqs. (35) and (36) to these initially prepared structures leads to fully relaxed twin structures, usually preserving the number of twins.

A. Strain and stress fields in austenite and martensite

Once the OP strain field which minimizes the total elastic energy of both the austenite and the martensite phases has been numerically determined, the compressional and shear strain fields in the inner domain and the three strain components in the outer domain can be obtained analytically. The strain fields in the outer domain are given by Eq. (16), whereas the expressions for the compressional and shear strain fields in the inner domain are given in Appendix B [Eq. (B12)]. In Fig. 5 we plot the three strain components of a fully relaxed twin structure in both the martensite and austenite phases for the geometry of Fig. 1 with periodic boundary conditions in the y direction to mimic a strip geometry. In this figure the matching planes cannot be distinguished from the habit planes. We obtain excellent matching of the three strain components, although as will be discussed below, at some points of the habit planes the compressional strain needs to be discontinuous. In addition, the compressional and shear strain fields within the martensite phase vanish far from the habit planes, as predicted by the bulk compatibility potential.[15] The twinned martensite structure matches the austenite phase at the (10) plane and generates an elastic fringing field on both sides of the habit planes.

The deviatoric stress $\sigma_2\equiv(\sigma_{xx}-\sigma_{yy})/\sqrt{2}=\partial f/\partial e_2$ at the habit plane obtained from the Ginzburg-Landau potential, f, from the austenite side is A_2e_2, whereas from the martensite side it is $A_2e_2-Be_2^3+Ce_2^5-\kappa\nabla^2e_2$. It is thus discontinuous at the habit plane as shown in Fig. 6(a). Since σ_{xx} needs to be continuous across the habit planes, as it is a component of the traction [see Eq. (18)], the discontinuity in σ_2 should arise from a discontinuity in σ_{yy} only. The discontinuity in σ_{yy} will also be reflected in the compressional stress, $\sigma_1\equiv(\sigma_{xx}+\sigma_{yy})/\sqrt{2}=\partial f/\partial e_1$. In Fig. 7 we plot the stress profiles in the [11] direction along (a) the center of a martensite plate and (b) at a twin boundary corresponding to the stress fields shown in Fig. 6. The discontinuity of the deviatoric, σ_2, and compressional, σ_1, stresses at the habit plane for case (a), along the center of the martensite plate in the [11] direction, can be clearly seen in Fig. 7(a), whereas $\sigma_{xx}=(\sigma_1+\sigma_2)/\sqrt{2}$ is continuous. Along the twin boundaries, the deviatoric stress is negligibly small, and thus a discontinuity cannot be observed. Hence, compressional stress [Fig. 7(b)] *appears* to be continuous. The stress fields σ_{xx} and σ_{yy} are also shown in Fig. 6. The discontinuity of σ_{yy} at the center of the martensite plate across the habit planes cannot be clearly seen as this stress component is much larger at the twin boundaries. The compressional, σ_1, and shear, $\sigma_3\equiv\sigma_{xy}$, stresses are not shown in this figure, as they are proportional to the corresponding strains, shown in Fig. 5. In the present work, all the continuity conditions have been imposed at the matching planes ($x=0$ and $x=L_2$), with no constraints on the habit planes, where there is the discontinuity of the Landau free energy. Therefore all the continuity/discontinuity relations at the habit planes are automatically obtained in the fully relaxed strain microstructures, with no assumptions other than elastic compatibility.

The discontinuity of the compressional stress σ_1 at the center of the martensite plates across the habit plane is also reflected in a discontinuity in the compressional strain, as $\sigma_1=A_1e_1$. This is shown in Fig. 8(a), where we plot the three strain profiles along the center of a martensite plate. The

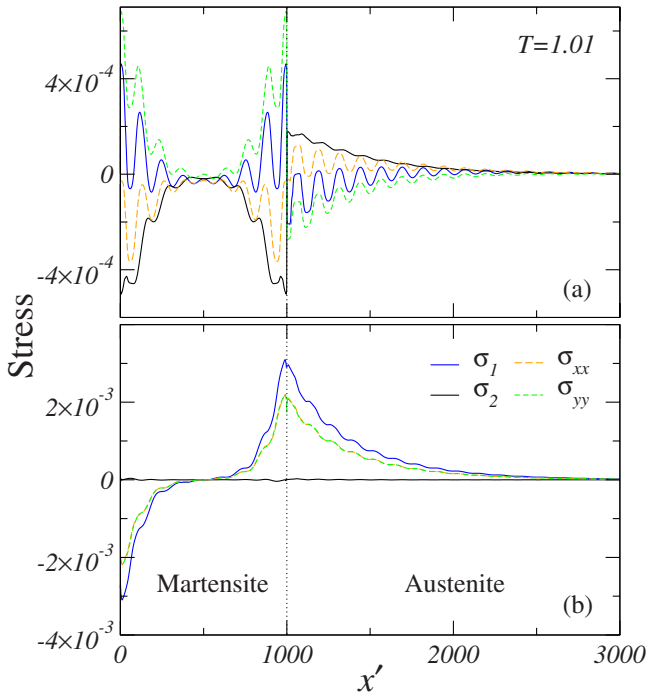

FIG. 7. (Color online) Stress profiles in the [11] direction along (a) the center of a martensite plate and (b) a twin boundary corresponding to the stress fields shown in Fig. 6. In (a) only σ_{xx} is continuous across the habit plane and in (b) σ_2 is very small so that σ_{xx} and σ_{yy} almost overlap, and the discontinuity in σ_{yy} and σ_1 is not apparent. The distance between the habit planes is $L=1000$.

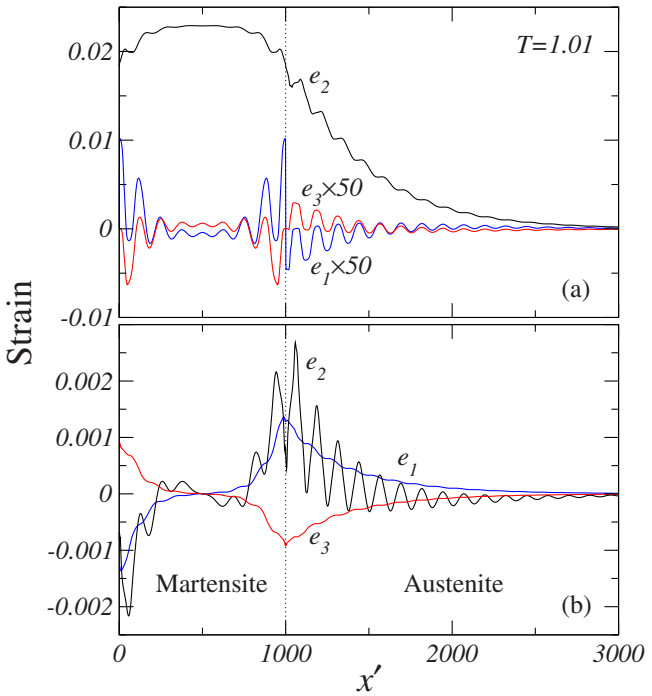

FIG. 8. (Color online) Strain profiles in the [11] direction along (a) the center of a martensite plate and (b) a twin boundary corresponding to the strain fields shown in Fig. 5. The compressional, e_1, and shear, e_3, strain fields in (a) are enlarged by a factor of 50 for clarity. The shear strain e_3 is continuous in both cases, whereas e_1 is discontinuous due to the discontinuity in σ_1. The distance between the habit planes is $L=1000$.

strain profiles along a twin boundary are shown in Fig. 8(b). In this figure it can also be seen that the shear strain is continuous across the habit planes in both cases, in Figs. 8(a) and 8(b). This is a necessary condition, as the shear stress, $\sigma_3=\sigma_{xy}=\frac{1}{2}A_3e_3$, is the other component of the traction. Given that in the martensite phase the Landau free energy is expanded up to the sixth order in the OP whereas it is only harmonic in the austenite phase, the matching of the OP strain, e_2, at the habit planes is exceptionally good. It is especially remarkable that the same oscillatory behavior is obtained on both sides of the habit planes. The periodicity of this oscillation is set by the dominant mode, k_y, in Eq. (16), which determines the twin width.

B. Length scaling properties of free energy and microstructure

An aspect of twinned martensite structure that has attracted attention, both experimentally[22,34,35] and theoretically[16,21–24] is the dependence of the twin width on the system size, i.e., in what sense is twinning a finite-size effect?. Using initial configurations with different numbers of twins, we obtain the elastic energy of fully relaxed twin structures as a function of the twin width, ξ, defined as the distance in the [10] direction between two neighboring twin boundaries. To show the scaling properties of the fringing field, we plot in Fig. 9 the elastic energy of the outer domain and the CS free energy of the inner domain per unit length of the habit plane as a function of the twin width, ξ, for different values of the distance between habit planes, L (for $L_2 \approx L$). As obtained analytically for deviatoric strain plane waves, both magnitudes scale as $F_{CS}^{\text{in}} \sim F^{\text{out}} \sim 1/|k_y| \sim \xi$ and are independent of the distance between habit planes. Therefore, in Fig. 9, the results corresponding to different values of L collapse onto a single straight line. The competition of these terms with the energy cost of the twin boundaries, which scales as $\sim LL_1/\xi$, determines an equilibrium value for the twin width. This is shown in Fig. 10, where we plot the

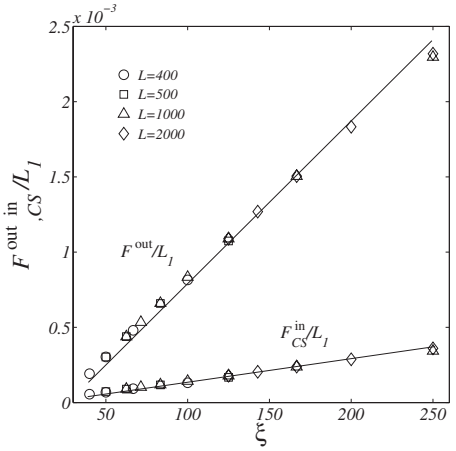

FIG. 9. Elastic energy of the outer domain and CS free energy of the inner domain per unit habit plane length as a function of the twin width for different values of the distance between habit planes, L ($\approx L_2$). The results correspond to $T=1.01$.

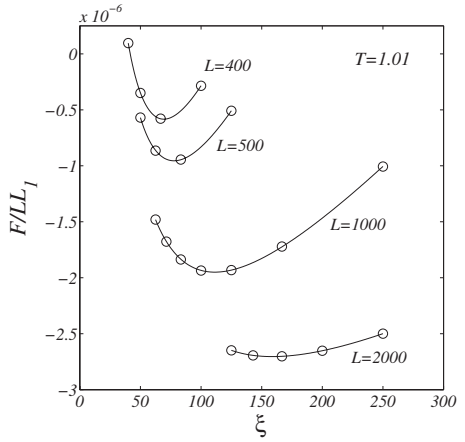

FIG. 10. Elastic energy of the sum of austenite and martensite phases per unit martensite area vs twin width (circles) for different values of the distance between habit planes, L. Solid lines are obtained by fitting the function $F=F_0+aL_1\xi+bLL_1/\xi$ to the numerical data. The results correspond to $T=1.01$.

total elastic energy (including austenite and martensite phases) per unit martensite area, LL_1, as a function of the twin width (circles), for different values of the distance between habit planes, L. Assuming that the contribution of the OP to the energy of the fringing field in the martensite phase also scales as $\sim 1/|k_y| \sim \xi$ and is independent of L, the total elastic energy as a function of the twin width has the functional form $F=F_0+aL_1\xi+bLL_1/\xi$, where F_0 is the free energy of a single variant martensite phase and an unstrained austenite phase, $aL_1\xi$ is the elastic energy of the fringing field at both sides of the habit planes, and bLL_1/ξ is the elastic energy of the twin boundaries (a and b are constants). The fit of this function (solid lines in Fig. 10) to the numerical data is excellent. From the minimum of these curves we obtain numerically the equilibrium twin width as a function of the distance between habit planes. This is shown in a log-log plot in Fig. 11 for the temperatures $T=1.002$, 1.01, and 1.02, between the stability limit of the austenite phase,

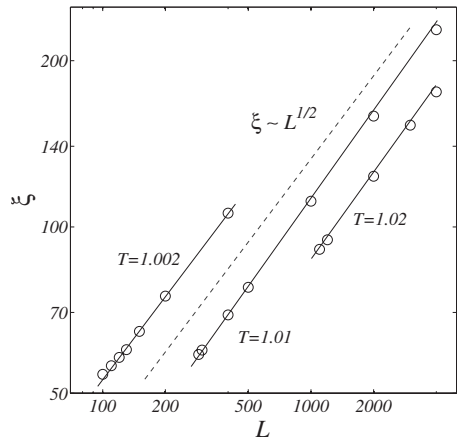

FIG. 11. Log-log plot of the equilibrium twin width vs the distance between habit planes, L (circles). The dashed line indicates the slope corresponding to the scaling law $\xi \sim \sqrt{L}$, and solid lines are guides to the eye.

$T_c=1$, and the temperature of the phase transition, $T_t=T_c+3B^2/(16AC)=1.0293$. The numerical results in Fig. 11 (circles) are consistent with the scaling relation $\xi \sim \sqrt{L}$ (dashed line) which follows from the function $F=F_0+aL_1\xi+bLL_1/\xi$, that is, $\xi=\sqrt{bL/a}$.

Thus, in a defect-free medium in which a large inclusion of martensite (L large) is surrounded by an austenite matrix, the microstructure will consist of coarse or wide twins with the energy of the system close to that of a single martensite variant. Additional results indicate that for L large, the decaying OP strain field, e_2, within the martensite phase is a universal function of the scaled position vector, $\mathbf{r}'/\xi$ (with respect to the habit plane),

$$e_2(x',y;\xi) = e_2^{\mathrm{mar}} + h(x'/\xi, y/\xi), \tag{37}$$

where e_2^{mar} is the value of the OP strain in the bulk martensite phase. Considering solely the fringing field emanating from the $x'=0$ habit plane, the associated elastic energy with respect to the single martensite variant scales as

$$\bar{F}_{OP}^{\mathrm{mar}} \sim \int_0^{L/2} dx' \int_0^{L_1} dy \bar{f}_{OP}^{\mathrm{mar}}[h(x'/\xi, y/\xi)], \tag{38}$$

where the OP free-energy density, $\bar{f}_{OP}^{\mathrm{mar}}[h]$, is written as a functional of the strain field $h(x'/\xi, y/\xi)$. The decaying function $h(x'/\xi, y/\xi)$ is negligibly small at a distance $x'/\xi=d$ from the habit plane. Thus, for $L>2d\xi$ the elastic energy in Eq. (38) can be expressed as

$$\bar{F}_{OP}^{\mathrm{mar}} \sim \int_0^{\infty} dx' \int_0^{L_1} dy \bar{f}_{OP}^{\mathrm{mar}}[h(x'/\xi, y/\xi)]$$

$$\sim \frac{L_1}{\xi} \int_0^{\infty} dx' \int_0^{\xi} dy \bar{f}_{OP}^{\mathrm{mar}}[h(x'/\xi, y/\xi)]. \tag{39}$$

Introducing the new variables $u=x'/\xi$ and $v=y/\xi$, we obtain

$$\bar{F}_{OP}^{\mathrm{mar}} \sim L_1\xi \int_0^{\infty} du \int_0^{1} dv \bar{f}_{OP}^{\mathrm{mar}}[h(u,v)]. \tag{40}$$

Since the function $h(u,v)$ does not depend on the twin width, ξ, or the distance between habit planes, L, the integral in Eq. (40) is a constant, and the elastic energy of the OP fringing field within the martensite phase behaves as $\bar{F}_{OP}^{\mathrm{mar}} \sim L_1\xi$, leading to the scaling relation $\xi \sim \sqrt{L}$. However, for $L<2d\xi$ the fringing fields emanating from each one of the habit planes overlap, and the resulting strain field no longer follows the universal function $h(x'/\xi, y/\xi)$. In this case, the integrals in Eq. (38) depend on L and the scaling law breaks down. This can be seen for $T=1.002$ and $L<150$ (Fig. 11) where the exponent ν of the scaling relation $\xi \sim L^{\nu}$ is $\nu=0.39<0.5$.

C. Nanoscale effects: size dependence of martensitic transition and microstructure

In order to explore questions related to how small an inclusion in an austenite matrix can support a martensite phase, we note that Fig. 10 gives us the elastic energy of the twinned martensite and the surrounding austenite matrix as a

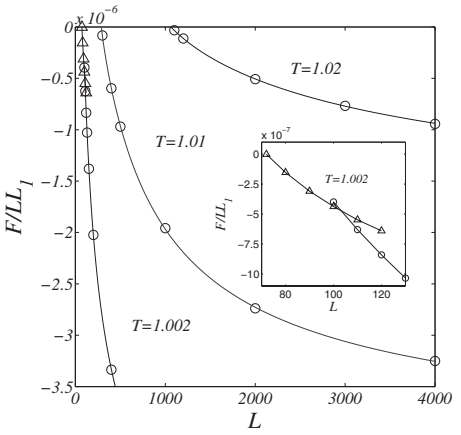

FIG. 12. Elastic energy of both the austenite and martensite phases per unit martensite area as a function of the distance between habit planes. Circles correspond to the twinned martensite structure, triangles to the lattice martensite, and lines are guides to the eye. The results corresponding to $T=1.002$ are enlarged in the inset.

function of the distance between habit planes. This is shown in Fig. 12 for the same three temperatures considered in Fig. 11 (circles). For large values of L the elastic free energy per unit martensite area decreases with increasing L toward the corresponding equilibrium value in the bulk (single variant), $F_0/(LL_1)$. For small values of L the result depends on the temperature. At the higher temperatures $T=1.01$ and 1.02 the free-energy density increases with decreasing L until it becomes positive for L smaller than a threshold $L^{\min}$, which depends on temperature. According to Eqs. (3)–(5) the elastic energy of a homogeneous austenite phase is zero. Therefore the nucleation of the twinned martensite is not energetically favorable for $L<L^{\min}$. At the lower temperature $T=1.002$, as L decreases the twinned martensite decays to a heterogeneous structure containing both the parent and product phases. This structure, which we refer to as *lattice martensite*, is shown in Fig. 13. It is a superposition of twins in $[11]$ and $[1\bar{1}]$ directions, and if no distinction is made between the different variants of the product phase, it can be regarded as a checker-board structure where parent and product phases alternate. The elastic energy of the lattice martensite structure as a function of L is also shown in Fig. 12 (triangles). The crossing of the curve corresponding to the twinned martensite (circles) with the curve corresponding to the lattice martensite (triangles) is enlarged in the inset. Therefore, at this temperature, as L decreases the structure exhibits a transition from the twinned martensite to the *lattice martensite*, and at lower values of L, to an unstrained austenite phase where martensite formation is arrested.

The reason for the stability of the LM structure is analyzed by evaluating the different contributions to the free energy in relation to the TM structure. This is done at $T=1.002$ and $L=100$, where the free energy of both structures is very similar (see the inset of Fig. 12). The results are shown in Table I. The different contributions to the free energy are the Landau free-energy expansion in the OP within the martensite region,

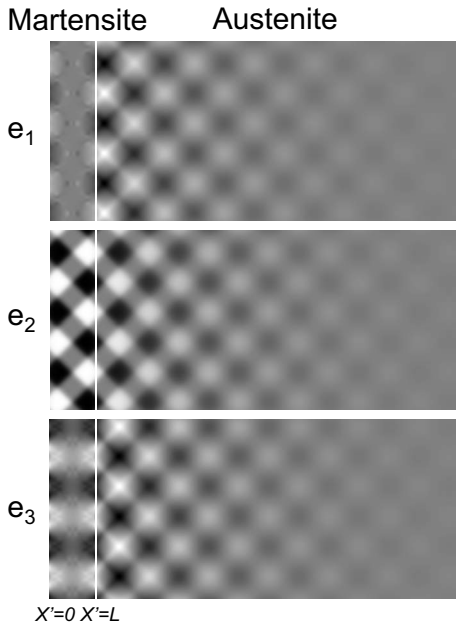

FIG. 13. Strain fields in the lattice martensite structure at $T=1.002$ and $L=100$. Grey corresponds to the unstrained (parent) structure, whereas black (white) corresponds to a negative (positive) strain.

$$F_L=\int_0^L dx'\int_0^{L_1} dy\left[\frac{A}{2}(T-T_c)e_2^2-\frac{B}{4}e_2^4+\frac{C}{6}e_2^6\right], \quad (41)$$

the gradient term,

$$F_G=\int_0^L dx'\int_0^{L_1} dy\frac{\kappa}{2}|\nabla e_2|^2, \quad (42)$$

the CS free energy within the martensite phase only,

TABLE I. Contributions to the elastic free energy in the twinned martensite (TM) and lattice martensite (LM) structures at $T=1.002$ and $L=100$. These are the Landau free energy in the martensite region, F_L, the gradient term, F_G, the compressional-shear free energy in the martensite region, F_{CS}^{mar}, and the elastic energy of the austenite phase, $F_{\text{aus}}^{\text{tot}}$. The total elastic energy, F, is given in the bottom row, and the energy difference between the lattice martensite and the twinned martensite structures is given in the right column. The LM structure is stabilized relative to the TM structure by F_G and $F_{\text{aus}}^{\text{tot}}$.

	TM	LM	LM-TM
F_L/L_1	-4.070×10^{-4}	-2.872×10^{-4}	1.198×10^{-4}
F_G/L_1	1.206×10^{-4}	5.92×10^{-5}	-6.13×10^{-5}
F_{CS}^{mar}/L_1	1.06×10^{-5}	4.1×10^{-6}	-6.5×10^{-6}
$F_{\text{aus}}^{\text{tot}}/L_1$	2.361×10^{-4}	1.801×10^{-4}	-5.59×10^{-5}
F/L_1	-3.99×10^{-5}	-4.37×10^{-5}	-3.8×10^{-6}

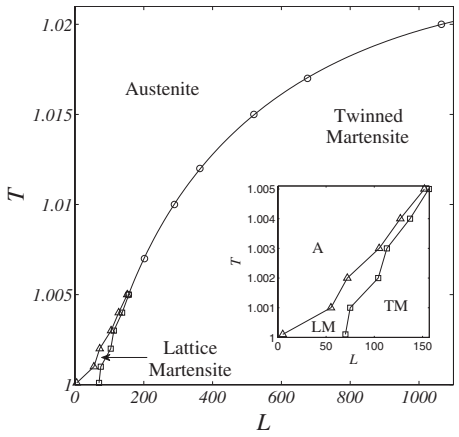

FIG. 14. Phase diagram of the martensite embedded in an austenite matrix. Circles indicate the minimum length for nucleation of the twinned martensite, triangles indicate the minimum length for nucleation of the lattice martensite, and squares indicate the transition from the lattice martensite to the twinned martensite. The region where the lattice martensite structure is stable is enlarged in the inset, and lines are guides to the eye ($100\ell \approx 24$ nm).

$$F_{CS}^{\mathrm{mar}} = \int_0^L dx' \int_0^{L_1} dy f_{CS}, \tag{43}$$

and the elastic energy of the whole austenite phase, including the small fraction of austenite within the inner domain (Fig. 1),

$$F_{\mathrm{aus}}^{\mathrm{tot}} = \int_{-\infty}^0 dx' \int_0^{L_1} dy f_{\mathrm{aus}} + \int_L^{+\infty} dx' \int_0^{L_1} dy f_{\mathrm{aus}}. \tag{44}$$

The total elastic energy, F, is given in the bottom row of Table I, and the energy difference between the lattice martensite and the twinned martensite structures is given in the right column. We obtain that the Landau free energy is lower for the twinned martensite structure, as the full transformable region ($L \times L_1$) is in the energetically favorable martensite phase, whereas in the lattice martensite structure, one half of the transformable region is in the austenite phase. On the contrary, the gradient term and the elastic energy of the austenite are lower in the lattice martensite structure. The CS free energy within the transformable region is also lower in the lattice martensite, but it is an order of magnitude smaller than the other terms. Thus, we conclude that the lattice martensite structure is stabilized with respect to the twinned martensite by the gradient term and the fringing fields within the austenite phase.

The equilibrium structures as a function of temperature and L are shown in Fig. 14. As a rule there is a minimum value of L for the nucleation of the twinned martensite. This minimum length depends on temperature and diverges as the transition temperature of the structural transformation, $T_t = 1.0293$, is approached. A characteristic feature of the twin microstructure as $T \to T_t$ already known in the literature[18,36] is the splitting of the rectangular-rectangular soliton into two square-rectangular solitons leading to the divergence of the width of the twin boundaries at the transition temperature, T_t. This is consistent with the divergence of the minimum length, $L^{\min}$, for nucleation of twinned martensite as $T \to T_t$. The lattice martensite structure, on the other hand, is stable for certain values of L for temperatures close to the *stability limit* of the austenite phase, $T_c = 1$, where the elastic constant associated with the order parameter of the phase transformation is very small or the system is very soft. From Table I it can be understood that the LM structure cannot be stable relative to the TM for large values of L, as the Landau term, which is dominant for large L, favors the TM structure.

It is worth noting that in the present work the gradient energy within the austenite phase has not been taken into account. This energy term is smaller for the LM structure than for the TM. Thus, we expect that if this term is considered, the region of the phase diagram where the LM is stable would be even larger.

VI. SHAPE-DEPENDENT MARTENSITE FORMATION

The results presented in the previous section were obtained for the geometry of Fig. 1 defined in Sec. II by minimizing the total energy, F, the sum of the austenite and martensite contributions. We consider here the microstructure formed as a result of other *finite* geometries and orientations.

In the geometry of Fig. 1, the martensite phase is infinite in the direction of the habit planes and the analytical results are only valid for this geometry. However, in the course of a structural phase transition, the nucleated martensite plates are finite. Hence, it is of interest to study the shape and microstructure of the nucleated martensite structure and pattern of fringing fields that result from a finite plate. We will correlate the microstructure with the plate geometry by performing simulations that include both the martensite plate, where the Landau free energy contains anharmonic terms in the OP, and the surrounding austenite matrix, where the Landau free energy is harmonic. The CS free energy is evaluated in both regions using the bulk compatibility potential,[15,16]

$$F_{CS}^{\mathrm{bulk}} = \frac{1}{2} \int d\mathbf{k} \frac{A_1 A_3 (k_x^2 - k_y^2)^2}{8 A_1 k_x^2 k_y^2 + A_3 (k_x^2 + k_y^2)^2} |\hat{e}_2(\mathbf{k})|^2, \tag{45}$$

where $\hat{e}_2(\mathbf{k})$ is the complex Fourier transform of $e_2(x,y)$. This is in contrast to our previous simulations that solved for the inner domain including the habit planes and where the effects of the outer domain were incorporated in the energy and boundary conditions at the matching planes. Of particular interest to us is the understanding of the lattice martensite structure that was discovered to be stable in a narrow region of the phase diagram (Fig. 14) since it combines both the austenite and the martensite phases and is a source of elastic heterogeneity. In Fig. 15(a) (left panel) we show the equilibrium strain field, e_2, obtained after minimization of the elastic energy when the martensite phase is allowed to nucleate in a sufficiently large square-shaped region oriented along the [11] direction. The same snapshot is shown in the right panel of Fig. 15(a) with the region where the martensite is allowed to nucleate plotted in white. The twinning direction is [11], consistent with $k_x = \pm k_y$ from bulk compatibility. Whereas there is almost perfect matching along the [11]

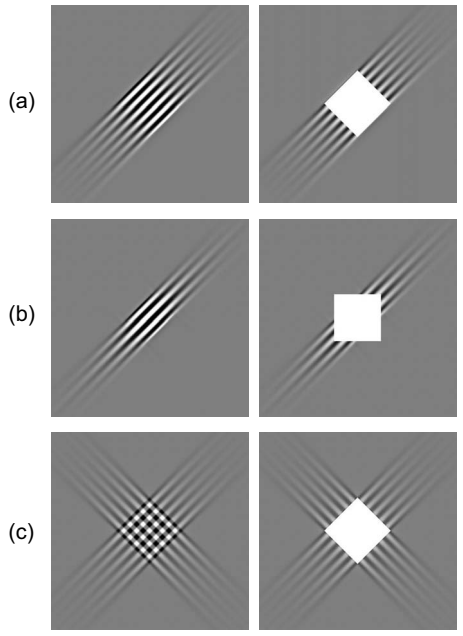

FIG. 15. (a) Fully relaxed equilibrium twinned martensite structure embedded in an austenite matrix obtained if the martensite phase is allowed to nucleate in a square region oriented in [11] direction (left panel). Grey corresponds to the unstrained (parent) structure whereas black (white) corresponds to a negative (positive) strain. In the right panel the same snapshot is shown, with the square region where the martensite phase is allowed to nucleate plotted in white. (b) Fully relaxed equilibrium twinned martensite structure embedded in an austenite matrix obtained if the martensite phase is allowed to nucleate in a square region oriented in [10] direction. (c) Fully relaxed metastable lattice martensite structure obtained if the martensite phase is allowed to nucleate in a square region oriented along [11] direction.

habit plane, the fringing fields decay along [11] across the $[\bar{1}1]$ habit planes (see Sec. II A). The equilibrium structure will either be twinned martensite or untransformed austenite if the square is not sufficiently large; however, the lattice martensite structure is never stabilized. In Fig. 15(b) we show that the same result as above is obtained from a square oriented along the [01] direction. The fact that the lattice martensite structure is not stabilized in these geometries can be understood by analyzing the fringing fields corresponding to the twinned martensite as compared to the fringing fields for the lattice martensite structure shown in Fig. 15(c) which was stabilized into a metastable state by not allowing it to reach the ground state in the absence of disorder. The fringing field corresponding to the lattice martensite structure (which varies smoothly across all four sides of the square) has a much larger energy than the fringing field of the twinned martensite structure [Fig. 15(a)]. In addition, in the nucleated lattice martensite only one half of the region is transformed into martensite, the other half is untransformed austenite. This structure is thus energetically unfavorable.

The reason for the nucleation of the lattice martensite structure (Fig. 13) in the geometry of Fig. 1 is that the elastic energy of the associated fringing field there is smaller than for the twinned martensite (Fig. 5) in the same geometry.

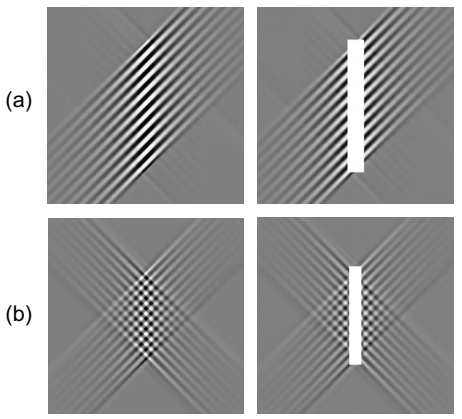

FIG. 16. (a) Fully relaxed equilibrium twinned martensite structure embedded in an austenite matrix obtained if the martensite phase is allowed to nucleate in a rectangular region of size $218.75\ell \times 1750\ell$ at $T=1.002$ (left panel). Grey corresponds to the unstrained (parent) structure whereas black (white) corresponds to a negative (positive) strain. In the right panel the same snapshot is shown, with the region where the martensite phase is allowed to nucleate plotted in white. (b) Fully relaxed equilibrium lattice martensite structure embedded in an austenite matrix obtained if the martensite phase is allowed to nucleate in a rectangular region of size $162.5\ell \times 1300\ell$ at $T=1.002$.

This is only possible if the intersections of the modulations corresponding to [11] and $[1\bar{1}]$ directions also occur within the austenite phase, reducing the elastic energy of the fringing field. We note that the intersections of the modes take place in the austenite for the infinite system (Fig. 13) but only in the transformed region for the finite geometry [Fig. 15(c)]. The crossing of the modes in [11] and $[1\bar{1}]$ directions within the austenite phase can also occur in a finite geometry if the region where the martensite phase is allowed to nucleate is rectangular rather than square and oriented along the [01] direction. Figure 16(a) shows a twinned martensite structure which has been stabilized if the martensite phase is allowed to nucleate in a region of dimensions $218.75\ell \times 1750\ell$ at $T=1.002$, where we recall that ℓ is the reduced unit of length, $\ell=\sqrt{\kappa/T_c A}=0.239\ 25$ nm. If the size of this region is reduced to $162.5\ell \times 1300\ell$, the stable structure changes to the lattice martensite [Fig. 16(b)]. The intersections of the modes resulting in the lattice structure in the fringing fields within the austenite are also seen, as are in the elastic fields within the martensite phase. Thus different geometries will have characteristic fringing field patterns that will be the result of the intersections of the diagonal modes.

The orientation required for the rectangular geometry to obtain the lattice martensite structure is the [01] direction, whereas in a SR structural phase transition the martensite plates are oriented in the [11] direction (Fig. 2). Hence, we do not expect to experimentally observe the lattice martensite structure in such a system. However, an elongated inclusion of a transformable material embedded in a nontransformable matrix (e.g., a nanocomposite) may show this behavior as the inclusion can be properly oriented along the [01] direction.

The lattice martensite structure obtained in the present model in confined geometries below the transition tempera-

ture, T_t, is closely related to the cross-hatched precursor modulations of the strain (tweed) observed above the transition temperature in the presence of disorder.[15] Whereas in the lattice martensite structure the confinement is due to a well-defined geometry, the tweed phenomenon may be considered to be the result of confinement due to the effects of disorder, giving rise to regions (nucleation centers) where locally the transition temperature is above the actual temperature, T. In this case, the crossing of the modes in [11] and $[1\bar{1}]$ directions in the fringing fields will not only occur due to the random geometry of the nucleation centers, but also due to the superposition of fringing fields emanating from different centers.

VII. SUMMARY AND DISCUSSION

The problem of determining the orientation of habit planes and twin boundaries has been addressed over several decades. Understanding under what conditions a given microstructure will be obtained is a more difficult task and has only been addressed more recently. Roytburd[11] studied how elastic interactions between domains lead to the formation of polydomain (alternating layers of domains) phases. Similarly, Horovitz *et al.*[21] considered the decaying displacement fields in austenite away from the habit plane, especially if continuity of the displacements must be satisfied, and showed how twinning can arise on the martensite side. They used a displacement based picture; however, the advent of energy minimizing simulations, especially in a strain-only-based formulation, now allows us to go beyond these previous studies by combining analytical results derived for strains with computer simulations. Hence, the nature of the strain fields and microstructure as a function of shapes and sizes of inclusions undergoing transformations when embedded in an austenite matrix can be obtained and the advantage of using strain is that the long-range anisotropic elastic interactions are explicitly taken into account in the minimization.

Our objective in this work is to solve the prototypical problem of coexisting austenite and martensite in the geometry shown in Fig. 1 that comprises a domain $L\times L_1$ with a habit plane of length L_1 along direction [01]. This is not the orientation of minimum energy for a parent/variant habit plane in an infinite system; however, it allows for the presence of fringing fields. We show in the austenite (outer domain) that the solution satisfying mechanical equilibrium, strain compatibility, and continuity across a matching plane leads to constraints on the strains at the matching planes and the energy scales as $1/|k_y|$. This shows that the austenite problem may be mapped to boundary conditions at the matching planes on the strains and their derivatives and that the energy would diverge unless the fraction of martensite variants in these planes was the same. The solution for the full austenite and martensite problem was until now not addressed; however, our approach to this problem merely requires the solution of the inner domain problem subject to the boundary conditions due to the outer domain. We are able to demonstrate that the energy also scales as $1/|k_y|$ and are able to perform simulations to obtain the microstructure and all strain fields, with the austenite fields given by the analytical solutions. Our work shows that when strain matching is not perfect, fringing fields develop and smoothly interpolate the deformations. Moreover, there is the same oscillatory behavior on both sides of the habit planes, a surprise as the local energy potentials are very different in the austenite and martensite.

We have been able to demonstrate the scaling of the energy with the width of twins and system size (for sufficiently large L) and the data provides an excellent fit to the functional form $F=F_0+aL_1\xi+bLL_1/\xi$ so that the width $\xi\sim\sqrt{L}$. As the system size L increases, coarser or wider twins become energetically more favored so that in the limit as $L\rightarrow\infty$, $F\rightarrow F_0$, the energy of one martensite variant. The other limit of how small can L be to support twinning leads to an enriched temperature-size phase diagram. We find that as L decreases, twinning is suppressed in favor of a stable phase consisting of both variants and untransformed austenite in a checker-board pattern that we refer to as *lattice martensite*. This occurs for temperatures close to the *stability limit* for austenite. Since our simulations use a [01] orientation for the habit plane, they could be observed in nanocomposites of crystals undergoing cubic-tetragonal or tetragonal-orthorhombic transformations oriented along [01] in an austenite matrix. Recently two-dimensional highly stable chessboard structure nanoscale patterns have been observed in $(Nd_{2/3-x}Li_{3x})TiO_3$, a perovskite-based lithium-ion conductor.[27] The patterns arise due to an interplay of a two-dimensional structural modulation and phase separation involving diffusion of the mobile Li^+ ion. The two-dimensional periodic separation leads to two compositionally distinct perovskite phases, one Li^+ rich and one relatively poor, with a repeat distance of 5–11 nm. The co-stabilization of the nanoscale phase separation satisfies short-range bonding requirements and alleviates a long-range instability such as a strain distortion. The number of interfaces between the different structural entities, within the constraints of the overall composition, is maximized—leading to the chessboard structure. Nanochecker-board patterns have also been fabricated in inorganic spinels such as $ZnMn_xGa_{2-x}O_4$, where the strain induced by the Jahn-Teller structural distortion is accompanied by diffusional phase separation of Mn^{3+}. The checker-board consists of four domains, two of which are the high-symmetry cubic and the other two are orthorhombic.[28] Although these systems differ from the lattice martensite structure in that there is diffusion of ions or phase separation, it is built on an underlying checker-board strain pattern. Whether the confinement of the strain field is the fundamental cause of the chessboard pattern, as in the lattice martensite, is not clear. Chessboard type patterns, consistent with those seen in experiments on Co-Pt alloys, have also been inferred in studies of coherent decomposition with several orientation variants of the precipitate phase.[29] The precipitation of the ordered tetragonal variants results from accommodation of the coherency strain. The chessboard is shown to arise from coupling of the concentration field of the precipitates with the elastic long-range interaction. The phenomenon occurs in bulk and is not a consequence of the elastic field confinement at the nanoscale.

Our results on the size effect are qualitatively consistent with the results of Waitz and co-workers[30] on the grain-size

dependence in NiTi alloys that undergo a martensitic transformation. For grains below 15 nm, only the parent B2 phase was observed and for grains larger than 150 nm, the lattice structure was consistent with that of the monoclinic B19' phase with twin widths of ~20 nm. The results illustrate the effects of confined geometry or boundary conditions as the grain size decreases and the effects on microstructure, aspects important in our study on a well-defined simpler model.

A study using atomistic simulations on the square-to-rectangle and cubic-to-tetragonal transformations would provide an independent test on the validity of our results and would be instructive in understanding the crossover, if any, from discrete to continuum behavior. Although experimental studies of nanocomposites of martensites in an austenite matrix are very few, the dependence of nucleation properties, such as activation barriers on the width of martensite layers of NiTi sandwiched between other materials have been studied.[37] Phase field models have also been used to study spinodal decomposition of binary alloys in constrained elastic films[38] and microstructure formation in layers of single variant martensite surrounded by austenite.[39] Similarly, the effects of thickness have been simulated in clamped martensites or layers of two different martensite materials.[40] The lattice martensite type of structure is observed in these studies; however, none of these derive effective boundary conditions at the interfaces due to the surrounding media examine fringing fields or strain accommodation across the interface or study energy or length scaling properties. In addition, the lattice martensite or checker-board pattern appears to be a generic feature of competing interactions among components in confined geometries as analogous patterns are seen in simulations of confined polymeric mixtures.[41]

A theory of nanocomposite behavior for ferroelastics calls for obtaining solutions of fringing fields and microstructure for different orientations in *finite* geometries of given size. In taking a step toward this problem, we have shown how full simulations allow us to understand the influence of shape and size in especially stabilizing the lattice martensite structure in the nanocomposite matrix, even outside the transformable region. Finally, it will be interesting to examine the effects of incompatibilities corresponding to dislocations, for example, on our analytical and numerical results as we have considered only defect-free media where the St. Venant compatibility constraint is enforced.

ACKNOWLEDGMENTS

This work was supported by CICyT (Spain) under Project No. MAT2007-61200, CIRIT (Catalonia) under Project No. 2005SGR00969, Marie-Curie RTN MULTIMAT (EU) under Contract No. MRTN-CT-2004-505226, DOE (U.S.), and NSERC (Canada). M.P. is thankful for the hospitality of the Theoretical Division at Los Alamos National Laboratory.

APPENDIX A: THE STRAIN FIELD IN THE OUTER DOMAIN INVOLVING AUSTENITE

In this appendix we derive the analytical expression for the strain field in the outer domain (at $x>0$) which arises from the coherent matching of the austenite to the martensite at the habit plane. We look for the strain field which minimizes the elastic energy of the outer domain, and at the same time satisfies continuity across the matching plane (at $x=0$). The minimization of the elastic energy with respect to the three strain components is achieved by demanding mechanical equilibrium. This is equivalent to requiring that the elastic force on each small volume of the system vanishes. In terms of the stress tensor, σ_{ij}, the force is given by

$$f_i = \sum_j \frac{\partial \sigma_{ij}}{\partial x_j}. \tag{A1}$$

In 2D this gives rise to two equations,

$$f_x = \partial_x \sigma_{xx} + \partial_y \sigma_{xy} = 0,$$

$$f_y = \partial_x \sigma_{yx} + \partial_y \sigma_{yy} = 0. \tag{A2}$$

The stress tensor is related to the elastic free-energy density, f, through

$$\sigma_{ij} = \frac{\partial f}{\partial \varepsilon_{ij}}. \tag{A3}$$

Thus, for the harmonic free energy corresponding to square symmetry [Eq. (5)] we obtain

$$A_1 \partial_x e_1 + A_2 \partial_x e_2 + \frac{A_3}{\sqrt{2}} \partial_y e_3 = 0,$$

$$A_1 \partial_y e_1 - A_2 \partial_y e_2 + \frac{A_3}{\sqrt{2}} \partial_x e_3 = 0. \tag{A4}$$

In addition, the strain field must satisfy elastic compatibility

$$(\partial_{xx} + \partial_{yy}) e_1 - (\partial_{xx} - \partial_{yy}) e_2 - \sqrt{8} \partial_{xy} e_3 = 0. \tag{A5}$$

Equations (A4) and (A5) together with the condition of continuity across the matching plane ($x=0$) and the requirement that the strain field vanishes far from this plane define a boundary-value problem. A straightforward, yet cumbersome, method of solving this problem is to transform the set of differential equations by Laplace in x direction and Fourier in y direction. This gives rise to the following set of algebraic equations:

$$A_1 [q\tilde{e}_1 - \hat{e}_1(0)] + A_2 [q\tilde{e}_2 - \hat{e}_2(0)] - ik_y \frac{A_3}{\sqrt{2}} \tilde{e}_3 = 0,$$

$$-ik_y A_1 \tilde{e}_1 + ik_y A_2 \tilde{e}_2 + \frac{A_3}{\sqrt{2}} [q\tilde{e}_3 - \hat{e}_3(0)] = 0,$$

$$(q^2 - k_y^2)\tilde{e}_1 - q\hat{e}_1(0) - \partial_x \hat{e}_1(0) - (q^2 + k_y^2)\tilde{e}_2 + q\hat{e}_2(0) + \partial_x \hat{e}_2(0) + ik_y \sqrt{8} [q\tilde{e}_3 - \hat{e}_3(0)] = 0, \tag{A6}$$

where the Fourier-Laplace transform is defined as

$$\tilde{e}_\alpha(q,k_y) = \frac{1}{L_1}\int_0^{L_1} e^{ik_y y}dy \int_0^{+\infty} e^{-qx} e_\alpha(x,y)dx, \quad \text{(A7)}$$

and $\hat{e}_\alpha(0)$ and $\partial_x\hat{e}_\alpha(0)$ are the Fourier transform with respect to y of the strain field and its derivative with respect to x, respectively, evaluated at the $x=0$ plane [see Eq. (12)].

From Eq. (A6) we obtain the Fourier-Laplace transform of the deviatoric strain field,

$$\tilde{e}_2(q,k_y) = \frac{1}{P(q)}\left\{\hat{e}_2(0)q^3 + \frac{1}{A_1+A_2}\left[\frac{i}{\sqrt{2}}A_3 k_y \hat{e}_3(0) - A_1[\partial_x\hat{e}_1(0) - \partial_x\hat{e}_2(0)]\right]q^2 - \frac{k_y^2}{(A_1+A_2)A_3} \times [2A_1(2A_1+A_3)\hat{e}_1(0) + [A_2(4A_1+A_3) - A_1A_3] \times \hat{e}_2(0)]q - \frac{k_y^2}{A_1+A_2}\left[i\sqrt{8}\left(A_1+\frac{1}{4}A_3\right)k_y\hat{e}_3(0) + A_1[\partial_x\hat{e}_1(0) - \partial_x\hat{e}_2(0)]\right]\right\}, \quad \text{(A8)}$$

where

$$P(q) = q^4 + 2\left[\frac{(A_1-A_2)A_3 - 4A_1A_2}{(A_1+A_2)A_3}\right]q^2k_y^2 + k_y^4. \quad \text{(A9)}$$

In order to obtain the deviatoric strain field in real space we must first perform the inverse Laplace transform of $\tilde{e}_2(q,k_y)$. To this end, it is convenient to write $\tilde{e}_2(q,k_y)$ as

$$\tilde{e}_2(q,k_y) = \frac{C_1}{q-r_1} + \frac{C_2}{q-r_2} + \frac{C_3}{q-r_3} + \frac{C_4}{q-r_4}, \quad \text{(A10)}$$

where r_i are the roots of the polynomial $P(q)$,

$$r_i = \pm k_y\sqrt{\frac{4A_1A_2 - (A_1-A_2)A_3 \pm 2\sqrt{A_1A_2\{4A_1A_2 - A_3[2(A_1-A_2)+A_3]\}}}{(A_1+A_2)A_3}}. \quad \text{(A11)}$$

Since the argument of the inner square root in Eq. (A11) is usually negative, the roots of the polynomial can be written in the form

$$r_i = \pm k_y\sqrt{X \pm iY}, \quad \text{(A12)}$$

where

$$X = \frac{4A_1A_2 - (A_1-A_2)A_3}{(A_1+A_2)A_3},$$

$$Y = \frac{2\sqrt{A_1A_2\{A_3[2(A_1-A_2)+A_3] - 4A_1A_2\}}}{(A_1+A_2)A_3}. \quad \text{(A13)}$$

Writing the complex number $X \pm iY$ in polar form we obtain

$$r_i = \pm k_y\sqrt{R}[\cos(\theta/2) \pm i\sin(\theta/2)], \quad \text{(A14)}$$

with $R=1$ and,

$$\sin(\theta/2) = \sqrt{A_1(A_3-2A_2)/A_3(A_1+A_2)} \equiv \beta. \quad \text{(A15)}$$

The four roots of the polynomial $P(q)$ can thus be written as

$$r_i = \pm k_y(C_\beta \pm i\beta), \quad \text{(A16)}$$

with $C_\beta \equiv \sqrt{1-\beta^2}$, or equivalently,

$$r_i = \pm |k_y|(C_\beta \pm i\beta). \quad \text{(A17)}$$

The Fourier-Laplace transform of the deviatoric strain field can therefore be written as

$$\tilde{e}_2(q,k_y) = \frac{C_1}{q-(C_\beta+i\beta)|k_y|} + \frac{C_2}{q-(C_\beta-i\beta)|k_y|} + \frac{C_3}{q-(-C_\beta+i\beta)|k_y|} + \frac{C_4}{q-(-C_\beta-i\beta)|k_y|}. \quad \text{(A18)}$$

Equating Eqs. (A8) and (A18) yields

$$C_1 = \frac{iC_\beta}{4\beta}\frac{A_1}{A_2}\hat{e}_1(0) + \frac{1}{4}\hat{e}_2(0) + \frac{i}{\sqrt{8}}\frac{1}{A_1+A_2}\frac{k_y}{|k_y|} \times \left(\frac{A_1+\frac{1}{2}A_3}{C_\beta} + \frac{i}{\beta}A_1\right)\hat{e}_3(0) + \frac{i}{4\beta}\frac{A_1}{A_1+A_2} \times \frac{1}{|k_y|}[\partial_x\hat{e}_1(0) - \partial_x\hat{e}_2(0)],$$

$$C_2 = -\frac{iC_\beta}{4\beta}\frac{A_1}{A_2}\hat{e}_1(0) + \frac{1}{4}\hat{e}_2(0) + \frac{i}{\sqrt{8}}\frac{1}{A_1+A_2}\frac{k_y}{|k_y|} \times \left(\frac{A_1+\frac{1}{2}A_3}{C_\beta} - \frac{i}{\beta}A_1\right)\hat{e}_3(0) - \frac{i}{4\beta}\frac{A_1}{A_1+A_2} \times \frac{1}{|k_y|}[\partial_x\hat{e}_1(0) - \partial_x\hat{e}_2(0)],$$

$$C_3 = -\frac{iC_\beta}{4\beta}\frac{A_1}{A_2}\hat{e}_1(0) + \frac{1}{4}\hat{e}_2(0) - \frac{i}{\sqrt{8}}\frac{1}{A_1+A_2}\frac{k_y}{|k_y|} \times \left(\frac{A_1+\frac{1}{2}A_3}{C_\beta} - \frac{i}{\beta}A_1\right)\hat{e}_3(0) + \frac{i}{4\beta}\frac{A_1}{A_1+A_2} \times \frac{1}{|k_y|}[\partial_x\hat{e}_1(0) - \partial_x\hat{e}_2(0)],$$

$$C_4 = \frac{iC_\beta}{4\beta}\frac{A_1}{A_2}\hat{e}_1(0) + \frac{1}{4}\hat{e}_2(0) - \frac{i}{\sqrt{8}}\frac{1}{A_1+A_2}\frac{k_y}{|k_y|} \times \left(\frac{A_1+\frac{1}{2}A_3}{C_\beta} + \frac{i}{\beta}A_1\right)\hat{e}_3(0) - \frac{i}{4\beta}\frac{A_1}{A_1+A_2} \times \frac{1}{|k_y|}[\partial_x\hat{e}_1(0) - \partial_x\hat{e}_2(0)], \quad \text{(A19)}$$

and performing the inverse Laplace transform of Eq. (A18) we obtain

$$\hat{e}_2(x) = C_1\exp[(C_\beta + i\beta)|k_y|x] + C_2\exp[(C_\beta - i\beta)|k_y|x] + C_3\exp[(-C_\beta + i\beta)|k_y|x] + C_4\exp[(-C_\beta - i\beta)|k_y|x]. \quad \text{(A20)}$$

The condition that the strain field vanishes far from the matching plane requires that $C_1=C_2=0$. We thus have two constraints on the strain field at this plane. These can be expressed as

$$\hat{e}_3(0) = \frac{i\sqrt{2}}{C_\beta}\frac{A_2}{A_3}\frac{k_y}{|k_y|}\hat{e}_2(0), \quad \text{(A21)}$$

and,

$$\partial_x\hat{e}_1(0) - \partial_x\hat{e}_2(0) = \frac{|k_y|}{A_3C_\beta}[-(2A_1+A_3)\hat{e}_1(0) + 2A_2\hat{e}_2(0)]. \quad \text{(A22)}$$

Using these relations, C_3 and C_4 simplify to

$$C_3 = -\frac{iC_\beta}{2\beta}\frac{A_1}{A_2}\hat{e}_1(0) + \frac{1}{2}\hat{e}_2(0),$$

$$C_4 = \frac{iC_\beta}{2\beta}\frac{A_1}{A_2}\hat{e}_1(0) + \frac{1}{2}\hat{e}_2(0), \quad \text{(A23)}$$

and the solution of the deviatoric strain field in real space in x direction and Fourier space in y direction is

$$\hat{e}_2(x) = \left[\frac{C_\beta}{\beta}\frac{A_1}{A_2}\hat{e}_1(0)\sin(\beta|k_y|x) + \hat{e}_2(0)\cos(\beta|k_y|x)\right] \times \exp(-C_\beta|k_y|x). \quad \text{(A24)}$$

Once the deviatoric strain field has been obtained, the computation of the compressional and shear strain fields becomes simpler. From Eq. (A6) we write the Fourier-Laplace transform of the compressional and shear strains in terms of the deviatoric strain,

$$\tilde{e}_1(q,k_y) = \frac{1}{(q^2+k_y^2)A_1}\left[-(q^2-k_y^2)A_2\tilde{e}_2(q,k_y) + (A_1\hat{e}_1(0) + A_2\hat{e}_2(0))q + \frac{i}{\sqrt{2}}A_3\hat{e}_3(0)k_y\right],$$

$$\tilde{e}_3(q,k_y) = \frac{i\sqrt{2}}{(q^2+k_y^2)A_3}\left[-2qk_yA_2\tilde{e}_2(q,k_y) + (A_1\hat{e}_1(0) + A_2\hat{e}_2(0))k_y - \frac{i}{\sqrt{2}}A_3\hat{e}_3(0)q\right]. \quad \text{(A25)}$$

The Fourier-Laplace transform of the deviatoric strain is given by Eq. (A18), with $C_1=C_2=0$, and C_3 and C_4 given by Eq. (A23). The Fourier-Laplace transform of the compressional and shear strain fields can thus be written as

$$\tilde{e}_1(q,k_y) = \frac{1}{q-(-C_\beta+i\beta)|k_y|}\left[\frac{1}{2}\hat{e}_1(0) + \frac{i}{2}\frac{A_2}{A_1}\frac{\beta}{C_\beta}\hat{e}_2(0)\right] + \frac{1}{q-(-C_\beta-i\beta)|k_y|}\left[\frac{1}{2}\hat{e}_1(0) - \frac{i}{2}\frac{A_2}{A_1}\frac{\beta}{C_\beta}\hat{e}_2(0)\right],$$

$$\tilde{e}_3(q,k_y) = \frac{1}{\sqrt{2}A_3}\frac{k_y}{|k_y|}\left\{\frac{1}{q-(-C_\beta+i\beta)|k_y|} \times \left[\frac{A_1}{\beta}\hat{e}_1(0) + i\frac{A_2}{C_\beta}\hat{e}_2(0)\right] + \frac{1}{q-(-C_\beta-i\beta)|k_y|} \times \left[-\frac{A_1}{\beta}\hat{e}_1(0) + i\frac{A_2}{C_\beta}\hat{e}_2(0)\right]\right\}. \quad \text{(A26)}$$

Performing the inverse Laplace transform yields

$$\hat{e}_1(x) = \left[\hat{e}_1(0)\cos(\beta|k_y|x) - \frac{\beta}{C_\beta}\frac{A_2}{A_1}\hat{e}_2(0)\sin(\beta|k_y|x)\right] \times \exp(-C_\beta|k_y|x),$$

$$\hat{e}_3(x) = \frac{i\sqrt{2}}{A_3}\frac{k_y}{|k_y|}\left[\frac{A_1}{\beta}\hat{e}_1(0)\sin(\beta|k_y|x) + \frac{A_2}{C_\beta}\hat{e}_2(0)\cos(\beta|k_y|x)\right] \times \exp(-C_\beta|k_y|x). \quad \text{(A27)}$$

APPENDIX B: THE ELASTIC ENERGY OF THE COMPRESSIONAL-SHEAR STRAIN FIELD IN THE INNER DOMAIN INVOLVING MARTENSITE

In this appendix we obtain the analytical expression of the compressional-shear strain field in the inner domain (Fig. 1) in terms of the deviatoric strain field. Its contribution to the elastic energy is then evaluated. Elastic compatibility [Eq. (2)], as well as the constraints at the matching planes obtained when deriving the elastic field in the outer domain [Eqs. (22)–(27)], are taken into account.

The appropriate transformation of the elastic compatibility equation in order to introduce the constraints at the matching planes is the complex Fourier transform in y direction and the cosine Fourier transform in x direction. This yields

$$\frac{2}{L_2}\int_0^{L_2}\cos\left(\frac{\pi n x}{L_2}\right)\partial_{xx}[\hat{e}_1(x)-\hat{e}_2(x)]dx+i\sqrt{8}k_y\frac{2}{L_2}\times\int_0^{L_2}\cos\left(\frac{\pi n x}{L_2}\right)\partial_x\hat{e}_3(x)dx-k_y^2[\hat{e}_1^{(n)}+\hat{e}_2^{(n)}]=0, \tag{B1}$$

where the complex-cosine Fourier transform is defined as

$$\hat{e}_{1,2}^{(n)}=\frac{2}{L_1L_2}\int_0^{L_1}e^{ik_y y}dy\int_0^{L_2}\cos\left(\frac{\pi n x}{L_2}\right)e_{1,2}(x,y)dx. \tag{B2}$$

Integration of Eq. (B1) by parts leads to

$$-(k_x^2+k_y^2)\hat{e}_1^{(n)}+(k_x^2-k_y^2)\hat{e}_2^{(n)}+i\sqrt{8}k_xk_y\hat{e}_3^{(n)}+\frac{2}{L_2}\{(-1)^n[\partial_x\hat{e}_1(L_2)-\partial_x\hat{e}_2(L_2)]-[\partial_x\hat{e}_1(0)-\partial_x\hat{e}_2(0)]\}+i\sqrt{8}k_y\frac{2}{L_2}[(-1)^n\hat{e}_3(L_2)-\hat{e}_3(0)]=0, \tag{B3}$$

where

$$\hat{e}_3^{(n)}=\frac{2}{L_2}\int_0^{L_2}\sin\left(\frac{\pi n x}{L_2}\right)\hat{e}_3(x)dx, \tag{B4}$$

and $k_x=\pi n/L_2$. We obtain that the integration constants depend on the derivative of the compressional strain and the value of the shear strain at the matching planes. These quantities have been obtained in terms of the deviatoric strain when the strain field at the outer domain has been derived [Eqs. (23), (24), (26), and (27)]. Introducing these expressions into Eq. (B3) we get

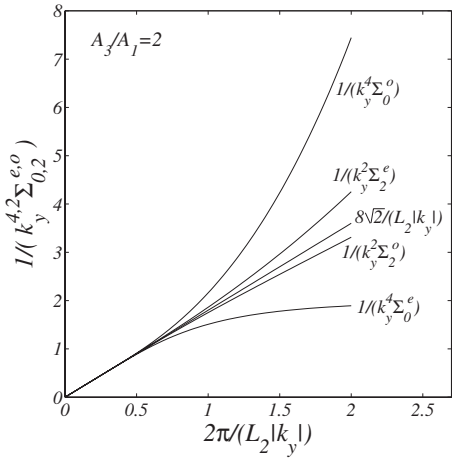

FIG. 17. Functions $1/(k_y^4\Sigma_0^{(n)})$ and $1/(k_y^2\Sigma_2^{(n)})$ as well as the corresponding expression in the continuum, $8\sqrt{(2A_1+A_3)/A_3}/(L_2|k_y|)$, *vs* $2\pi/(L_2|k_y|)$ for $A_3/A_1=2$.

$$-(k_x^2+k_y^2)\hat{e}_1^{(n)}+(k_x^2-k_y^2)\hat{e}_2^{(n)}+i\sqrt{8}k_xk_y\hat{e}_3^{(n)}-\frac{2}{L_2}\frac{|k_y|}{C_\beta}\frac{A_2(4A_1+A_3)}{A_1A_3}\Gamma^{(n)}+\frac{2}{L_2}\frac{A_1+A_2}{A_1}\Delta^{(n)}=0, \tag{B5}$$

where $\Gamma^{(n)}$ and $\Delta^{(n)}$ are functions of the deviatoric strain field at the matching planes,

$$\Gamma^{(n)}\equiv\hat{e}_2(0)+(-1)^n\hat{e}_2(L_2),$$

$$\Delta^{(n)}\equiv\partial_x\hat{e}_2(0)-(-1)^n\partial_x\hat{e}_2(L_2). \tag{B6}$$

Notice that since $\hat{e}_3^{(n)}$ are the coefficients of the sine Fourier expansion of $\hat{e}_3(x)$, they do not contain information of the value of the shear strain at the matching planes. For the same reason, the coefficients of the cosine Fourier expansion of $\hat{e}_1(x)$ and $\hat{e}_1^{(n)}$ do not contain information of the derivative of the compressional strain at the matching planes. This information has been introduced into the elastic compatibility equation [Eq. (B5)] through the integration constants. On the contrary, the information of the value of the compressional strain at the matching planes is indeed contained in the coefficients $\hat{e}_1^{(n)}$, and it has not been required to determine the integration constants of the elastic compatibility equation. Therefore, the constraints on the value of the compressional strain at the matching planes [Eqs. (22) and (25)] must be imposed on the coefficients $\hat{e}_1^{(n)}$. Using the expansion

$$\hat{e}_1(x)=\frac{1}{2}\hat{e}_1^{(0)}+\sum_{n=1}^{\infty}\hat{e}_1^{(n)}\cos\left(\frac{\pi n x}{L_2}\right), \tag{B7}$$

Eqs. (22) and (25) can be written as

$$\frac{1}{2}\hat{e}_1^{(0)}+\sum_{n=1}^{\infty}\hat{e}_1^{(n)}=\frac{A_2}{A_1}\left[\hat{e}_2(0)-\frac{1}{C_\beta|k_y|}\partial_x\hat{e}_2(0)\right],$$

$$\frac{1}{2}\hat{e}_1^{(0)}+\sum_{n=1}^{\infty}(-1)^n\hat{e}_1^{(n)}=\frac{A_2}{A_1}\left[\hat{e}_2(L_2)+\frac{1}{C_\beta|k_y|}\partial_x\hat{e}_2(L_2)\right]. \tag{B8}$$

Summation and subtraction of these equations leads to a more convenient form of the constraints on the compressional strain field,

$$\hat{e}_1^{(0)}+2\sum_{n\ \text{even}(\neq 0)}\hat{e}_1^{(n)}=\frac{A_2}{A_1}\left[\Gamma^{(0)}-\frac{1}{C_\beta|k_y|}\Delta^{(0)}\right],$$

$$2\sum_{n\ \text{odd}}\hat{e}_1^{(n)}=\frac{A_2}{A_1}\left[\Gamma^{(1)}-\frac{1}{C_\beta|k_y|}\Delta^{(1)}\right]. \tag{B9}$$

In order to obtain an expression for the compressional and shear strain fields in terms of the deviatoric strain field alone, we need to minimize the elastic energy of the inner domain with respect to these fields, taking into account elastic compatibility and the constraints at the matching planes.

In Fourier space the compressional-shear free energy of the inner domain [Eqs. (4) and (28)] is given by

$$F_{CS}^{\text{in}} = L_1 \sum_{k_y} \left[\frac{1}{2} A_1 \left(\frac{L_2}{4} \hat{e}_1^{(0)} \hat{e}_1^{(0)*} + \frac{L_2}{2} \sum_{n=1}^{\infty} \hat{e}_1^{(n)} \hat{e}_1^{(n)*} \right) + \frac{1}{2} A_3 \left(\frac{L_2}{2} \sum_{n=1}^{\infty} \hat{e}_3^{(n)} \hat{e}_3^{(n)*} \right) \right]. \tag{B10}$$

The compressional strain field can be written in terms of the deviatoric and shear strain fields using elastic compatibility [Eq. (B5)]. In this way, the compressional-shear free energy of the inner domain only has to be minimized with respect to the shear strain, taking into account the constraints given by Eq. (B9). Introducing the Lagrangian multipliers $\lambda(k_y)$ and $\mu(k_y)$, the function to be minimized with respect to the shear strain is, therefore,

$$G = F_{CS}^{\text{in}} + \sum_{k_y} \lambda(k_y) \left\{ \hat{e}_1^{(0)} + 2 \sum_{n \text{ even}(\neq 0)} \hat{e}_1^{(n)} - \frac{A_2}{A_1} \left[\Gamma^{(0)} - \frac{1}{C_\beta |k_y|} \Delta^{(0)} \right] \right\} + \sum_{k_y} \mu(k_y) \times \left\{ 2 \sum_{n \text{ odd}} \hat{e}_1^{(n)} - \frac{A_2}{A_1} \left[\Gamma^{(1)} - \frac{1}{C_\beta |k_y|} \Delta^{(1)} \right] \right\}. \tag{B11}$$

The result is

$$\hat{e}_1^{(n)} = \frac{A_3}{8A_1 k_x^2 k_y^2 + A_3 (k_x^2 + k_y^2)^2} \left\{ (k_x^2 - k_y^2)(k_x^2 + k_y^2) \hat{e}_2^{(n)} - \frac{k_x^2}{\Sigma_2^{(n)}} \Sigma_\alpha^{(n)} + \frac{A_2}{A_1} \frac{1}{\Sigma_2^{(n)}} \left[\frac{k_x^2}{2} - \frac{2k_y^2 |k_y|}{L_2} \frac{4A_1 + A_3}{A_3 C_\beta} (\Sigma_2^{(n)} - k_x^2 \Sigma_0^{(n)}) \right] \Gamma^{(n)} + \frac{1}{A_1} \frac{1}{\Sigma_2^{(n)}} \left[-\frac{k_x^2}{2|k_y|} \frac{A_2}{C_\beta} + \frac{2k_y^2}{L_2} (A_1 + A_2)(\Sigma_2^{(n)} - k_x^2 \Sigma_0^{(n)}) \right] \Delta^{(n)} \right\},$$

$$\hat{e}_3^{(n)} = \frac{A_3}{8A_1 k_x^2 k_y^2 + A_3 (k_x^2 + k_y^2)^2} \left\{ i\sqrt{8} \frac{A_1}{A_3} k_x k_y (k_x^2 - k_y^2) \hat{e}_2^{(n)} + \frac{ik_x (k_x^2 + k_y^2)}{\sqrt{8} k_y \Sigma_2^{(n)}} \Sigma_\alpha^{(n)} + \frac{i\sqrt{8}(k_x^2 + k_y^2)}{\Sigma_2^{(n)}} \frac{A_2}{A_1} \times \left[-\frac{k_x}{16k_y} + \frac{k_y |k_y|}{L_2} \frac{4A_1 + A_3}{4A_3 C_\beta} \left(\frac{1}{k_x} \Sigma_2^{(n)} - k_x \Sigma_0^{(n)} \right) \right] \Gamma^{(n)} + \frac{i\sqrt{8}(k_x^2 + k_y^2)}{A_1 \Sigma_2^{(n)}} \left[\frac{k_x}{16k_y |k_y|} \frac{A_2}{C_\beta} - \frac{k_y (A_1 + A_2)}{4L_2} \times \left(\frac{1}{k_x} \Sigma_2^{(n)} - k_x \Sigma_0^{(n)} \right) \right] \Delta^{(n)} \right\} - \frac{i\sqrt{8}|k_y|}{L_2 k_x k_y} \frac{A_2}{A_1 A_3} \frac{4A_1 + A_3}{4C_\beta} \Gamma^{(n)} + \frac{i\sqrt{8}}{4L_2 k_x k_y} \frac{A_1 + A_2}{A_1} \Delta^{(n)}, \tag{B12}$$

where

$$\Sigma_\alpha^{(n)} = \begin{cases} -\frac{1}{2} \hat{e}_2^{(0)} + \sum_{m \text{ even}(\neq 0)} \frac{A_3 (\bar{k}_x^2 - k_y^2)(\bar{k}_x^2 + k_y^2)}{8A_1 \bar{k}_x^2 k_y^2 + A_3 (\bar{k}_x^2 + k_y^2)^2} \hat{e}_2^{(m)} \equiv \Sigma_\alpha^e, & n \text{ even} \\ \sum_{m \text{ odd}} \frac{A_3 (\bar{k}_x^2 - k_y^2)(\bar{k}_x^2 + k_y^2)}{8A_1 \bar{k}_x^2 k_y^2 + A_3 (\bar{k}_x^2 + k_y^2)^2} \hat{e}_2^{(m)} \equiv \Sigma_\alpha^o, & n \text{ odd}, \end{cases}$$

$$\Sigma_0^{(n)} = \begin{cases} \frac{1}{2k_y^4} + \sum_{m \text{ even}(\neq 0)} \frac{A_3}{8A_1 \bar{k}_x^2 k_y^2 + A_3 (\bar{k}_x^2 + k_y^2)^2} \equiv \Sigma_0^e, & n \text{ even} \\ \sum_{m \text{ odd}} \frac{A_3}{8A_1 \bar{k}_x^2 k_y^2 + A_3 (\bar{k}_x^2 + k_y^2)^2} \equiv \Sigma_0^o, & n \text{ odd}, \end{cases}$$

$$\Sigma_2^{(n)} = \begin{cases} \sum_{m \text{ even}(\neq 0)} \frac{A_3 \bar{k}_x^2}{8A_1 \bar{k}_x^2 k_y^2 + A_3 (\bar{k}_x^2 + k_y^2)^2} \equiv \Sigma_2^e, & n \text{ even} \\ \sum_{m \text{ odd}} \frac{A_3 \bar{k}_x^2}{8A_1 \bar{k}_x^2 k_y^2 + A_3 (\bar{k}_x^2 + k_y^2)^2} \equiv \Sigma_2^o, & n \text{ odd}, \end{cases} \tag{B13}$$

and $\bar{k}_x = \pi m / L_2$. Introducing these expressions into Eq. (B10) the compressional-shear free energy of the inner domain can be written as

$$F_{CS}^{\text{in}} = \frac{L_1 L_2}{2} \sum_{k_y} \left\{ \frac{A_1}{4} \left| -\hat{e}_2^{(0)} + \frac{1}{|k_y| L_2} \Phi^{(0)} \right|^2 + \sum_{n \neq 0} \frac{\frac{1}{2} A_1 A_3}{8 A_1 k_x^2 k_y^2 + A_3 (k_x^2 + k_y^2)^2} \left| (k_x^2 - k_y^2) \hat{e}_2^{(n)} + \frac{|k_y|}{L_2} \Phi^{(n)} \right|^2 + \frac{A_3}{16 k_y^2} \left[\frac{1}{\Sigma_2^e} |\Sigma_\alpha^e + \Psi^e|^2 + \frac{1}{\Sigma_2^o} |\Sigma_\alpha^o + \Psi^o|^2 \right] \right\}, \tag{B14}$$

where $\Phi^{(n)}$, Ψ^e, and Ψ^o are functions of the deviatoric strain and its gradient at the matching planes,

$$\Phi^{(n)} = -\frac{2A_2(4A_1 + A_3)}{A_1 A_3 C_\beta} \Gamma^{(n)} + \frac{2(A_1 + A_2)}{A_1 |k_y|} \Delta^{(n)},$$

$$\Psi^e = -\frac{A_2}{A_1} \left[\frac{1}{2} + \frac{2|k_y|}{L_2 C_\beta} \frac{4A_1 + A_3}{A_3} (\Sigma_2^e + k_y^2 \Sigma_0^e) \right] \Gamma^{(0)} + \frac{1}{A_1} \left[\frac{A_2}{2|k_y| C_\beta} + \frac{2(A_1 + A_2)}{L_2} (\Sigma_2^e + k_y^2 \Sigma_0^e) \right] \Delta^{(0)},$$

$$\Psi^o = -\frac{A_2}{A_1} \left[\frac{1}{2} + \frac{2|k_y|}{L_2 C_\beta} \frac{4A_1 + A_3}{A_3} (\Sigma_2^o + k_y^2 \Sigma_0^o) \right] \Gamma^{(1)} + \frac{1}{A_1} \left[\frac{A_2}{2|k_y| C_\beta} + \frac{2(A_1 + A_2)}{L_2} (\Sigma_2^o + k_y^2 \Sigma_0^o) \right] \Delta^{(1)}. \tag{B15}$$

In the present work the numerical results of the compressional-shear free energy of the inner domain correspond to the expression given in Eqs. (B14) and (B15). Nevertheless, for the analysis of these equations it may be convenient to obtain an approximate analytical expression for the summations Σ_0^e, Σ_0^o, Σ_2^e, and Σ_2^o. These can be approximated by

$$\Sigma_0^e \approx \Sigma_0^o \approx \frac{L_2}{2\pi} \int_0^\infty \frac{A_3 dk_x}{8A_1 k_x^2 k_y^2 + A_3 (k_x^2 + k_y^2)^2} = \frac{L_2}{8|k_y|^3} \sqrt{\frac{A_3}{2A_1 + A_3}},$$

$$\Sigma_2^e \approx \Sigma_2^o \approx \frac{L_2}{2\pi} \int_0^\infty \frac{A_3 k_x^2 dk_x}{8A_1 k_x^2 k_y^2 + A_3 (k_x^2 + k_y^2)^2} = \frac{L_2}{8|k_y|} \sqrt{\frac{A_3}{2A_1 + A_3}}. \tag{B16}$$

In order to check the validity of this approximation in Fig. 17 we plot the functions $1/(k_y^4 \Sigma_0^{(n)})$ and $1/(k_y^2 \Sigma_2^{(n)})$ as well as the corresponding expression from Eq. (B16) *vs* $2\pi/(L_2|k_y|)$ for $A_3/A_1 = 2$. The approximation is good for $|k_y| \gg 2\pi/L_2$, that is, for modulation wavelengths in y direction much shorter than the distance between matching planes. Introducing these expressions into Eqs. (B14) and (B15) we obtain the expressions given in Eqs. (30) and (31).

[1] K. Bhattacharya, *Microstructure of Martensite* (Oxford University Press, Oxford, 2003).
[2] E. K. H. Salje, *Phase Transitions in Ferroelastic and Co-elastic Crystals* (Cambridge University Press, Cambridge, 1990).
[3] A. G. Khachaturyan, *Theory of Structural Transformations in Solids* (Wiley, New York, 1983).
[4] *Shape Memory Materials*, edited by K. Otsuka and C. M. Wayman (Cambridge University Press, Cambridge, 1998).
[5] *Intrinsic Multiscale Structure and Dynamics in Complex Electronic Oxides*, edited by A. R. Bishop, S. R. Shenoy, and S. Sridhar (World Scientific, Singapore, 2003).
[6] N. Mathur and P. Littlewood, Phys. Today **56**(1), 25 (2003).
[7] K. H. Ahn, T. Lookman, and A. R. Bishop, Nature (London) **428**, 401 (2004).
[8] H. Y. Hwang, T. T. M. Palstra, S.-W. Cheong, and B. Batlogg, Phys. Rev. B **52**, 15046 (1995).
[9] K. Aizu, J. Phys. Soc. Jpn. **27**, 387 (1969).
[10] J. Dec, Phase Transitions **45**, 35 (1993).
[11] A. L. Roytburd, Phase Transitions **45**, 1 (1993).
[12] A. Moore, J. Graham, G. K. Williamson, and G. V. Raynor, Acta Metall. **3**, 579 (1955).
[13] G. R. Barsch and J. A. Krumhansl, Phys. Rev. Lett. **53**, 1069 (1984).
[14] J. M. Ball and R. D. James, Arch. Ration. Mech. Anal. **100**, 13 (1987).
[15] S. Kartha, J. A. Krumhansl, J. P. Sethna, and L. K. Wickham, Phys. Rev. B **52**, 803 (1995).
[16] T. Lookman, S. R. Shenoy, K. Ø. Rasmussen, A. Saxena, and A. R. Bishop, Phys. Rev. B **67**, 024114 (2003); S. R. Shenoy, T. Lookman, A. Saxena, and A. R. Bishop, *ibid.* **60**, R12537 (1999).
[17] F. Falk, Z. Phys. B: Condens. Matter **51**, 177 (1983).
[18] A. E. Jacobs, Phys. Rev. B **31**, 5984 (1985).
[19] J. Sapriel, Phys. Rev. B **12**, 5128 (1975).
[20] D. M. Hatch, T. Lookman, A. Saxena, and S. R. Shenoy, Phys. Rev. B **68**, 104105 (2003).
[21] B. Horovitz, G. R. Barsch, and J. A. Krumhansl, Phys. Rev. B **43**, 1021 (1991).
[22] G. Arlt, D. Hennings, and G. de With, J. Appl. Phys. **58**, 1619 (1985).
[23] T. E. Mitchell and J. P. Hirth, Acta Metall. Mater. **39**, 1711 (1991).
[24] A. G. Khachaturyan and G. A. Shatalov, Sov. Phys. JETP **29**, 557 (1969).
[25] M. Rao and S. Sengupta, Phys. Rev. Lett. **78**, 2168 (1997).
[26] M. Baus and R. Lovett, Phys. Rev. Lett. **65**, 1781 (1990).
[27] B. S. Guiton and P. K. Davies, Nature Mater. **6**, 586 (2007).
[28] S. Yeo, Y. Horibe, S. Mori, C. M. Tseng, C. H. Chen, A. G. Khachaturyan, C. L. Zhang, and S.-W. Cheong, Appl. Phys. Lett. **89**, 233120 (2006).
[29] Y. Le Bouar, A. Loiseau, and A. G. Khachaturyan, Acta Mater. **46**, 2777 (1998).
[30] T. Waitz and H. P. Karnthaler, Acta Mater. **52**, 5461 (2004); T. Waitz, *ibid.* **53**, 2273 (2005); T. Waitz, T. Antretter, F. D. Fis-

cher, N. K. Simha, and H. P. Karnthaler, J. Mech. Phys. Solids **55**, 419 (2007); T. Waitz, W. Pranger, T. Antretter, F. D. Fischer, and H. P. Karnthaler, Mater. Sci. Eng., A **481-482**, 479 (2008).
[31] L. D. Landau and E. M. Lifshitz, *Theory of Elasticity*, 3rd ed. (Butterworth-Heinemann, Oxford, 1986).
[32] Y. C. Fung, *A First Course in Continuum Mechanics* (Prentice-Hall, New Jersey, 1977).
[33] To obtain this scaling relation the results $\Sigma_n A_3/[8A_1k_x^2k_y^2 + A_3(k_x^2+k_y^2)^2] \sim L_2/|k_y|^3$ and $\Sigma_n A_3 k_x^2/[8A_1k_x^2k_y^2+A_3(k_x^2+k_y^2)^2] \sim L_2/|k_y|$ are needed (see Appendix B).
[34] L. S. Chumbley, J. D. Verhoeven, M. R. Kim, A. L. Cornelius, and M. J. Kramer, IEEE Trans. Magn. **25**, 2337 (1989).
[35] T. Roy and T. E. Mitchell, Philos. Mag. A **63**, 225 (1991).
[36] J. Lajzerowicz, Ferroelectrics **35**, 219 (1981).
[37] X. Wang, M. Rein, and J. J. Vlassak, J. Appl. Phys. **103**, 023501 (2008).
[38] D. J. Seol, S. Y. Hu, Y. L. Li, J. Shen, K. H. Oh, and L. Q. Chen, Acta Mater. **51**, 5173 (2003).
[39] A. Artemev, J. Slutsker, and A. L. Roytburd, Acta Mater. **53**, 3425 (2005).
[40] M. Bouville and R. Ahluwalia, Phys. Rev. B **79**, 094110 (2009).
[41] A. Karim, J. F. Douglas, B. P. Lee, S. C. Glotzer, J. A. Rogers, R. J. Jackman, E. J. Amis, and G. M. Whitesides, Phys. Rev. E **57**, R6273 (1998).